UNIVERSITY OF CALIFORNIA
RIVERSIDE

# Noncuring Thermal Interface Materials with Graphene Fillers for Thermal Management of Concentrated Photovoltaic Solar Cells

A Thesis submitted in partial satisfaction
of the requirements for the degree of

Master of Science

in

Materials Science and Engineering

by

Barath Kanna Mahadevan

March 2020

Thesis Committee:
Dr. Alexander A.Balandin, Chairperson
Dr. Fariborz Kargar
Dr. Lorenzo Mangolini

The Thesis of Barath Kanna Mahadevan is approved by:

---

---

---

Committee Chairperson

University of California, Riverside

# Acknowledgements

Firstly, I would like to express my very sincere gratitude and appreciation to my advisor, Dr. Alexander A. Balandin, for giving me the opportunity to work under his supervision and providing valuable support and advice for my courses, research and future career throughout my master's study. I would also like express my sincere gratitude to Dr. Fariborz Kargar for his guidance, motivation and immense support for my research and I thank him for serving on my thesis committee. I would like to thank Dr. Lorenzo Mangolini for serving on my thesis committee. It has been my honor to be a part of Phonon Optimized Engineered Materials (POEM) Lab working with such smart, active, friendly and helping lab members. I would especially like to thank Dr. Ruben Salgado, Dr. Sahar Naghibi and Amirmahdi Mohammadzadeh for their support for my research. I would like to thank University of California – Riverside, Materials Science and Engineering discipline, for giving me the opportunity to be a part of this beautiful institute. Last but not the least, I would like to thank my parents, teachers and friends for their immense support and trust throughout these years.

This thesis work was supported, in part, by the UC – National Laboratory Collaborative Research and Training Program. The text of this thesis, in part, is a reprint of the material as it appears in Mahadevan, B.K.; Naghibi, S.; Kargar, F.; Balandin, A.A. Non-Curing Thermal Interface Materials with Graphene Fillers for Thermal Management of Concentrated Photovoltaic Solar Cells. C—Journal of Carbon Research. 2019, 6, 2. The co-author Dr. Alexander A.Balandin listed in that publication directed and supervised the research which forms the basis for this thesis.

The figures of this thesis, in part, is a reproduction of work copyrighted by someone else with permission to include, as it appears in:

- Dimroth, F.; Kurtz, S. High-Efficiency Multijunction Solar Cells. *MRS Bulletin* **2007**, *32*, 230–235.
- Riordan, C.; Hulstrom, R. What is an Air Mass 1.5 Spectrum? *IEEE Photovoltaic Specialists Conferenc*e, Kissimmee, FL, USA **1990**, *2*, 1085–1088.

ABSTRACT OF THE THESIS

Noncuring Thermal Interface Materials with Graphene Fillers for Thermal Management of Concentrated Photovoltaic Solar Cells

by

Barath Kanna Mahadevan

Master of Science, Graduate Program in Materials Science and Engineering
University of California, Riverside, March 2020
Dr. Alexander A. Balandin, Chairperson

Temperature rise in multi-junction solar cells reduces their efficiency and shortens their lifetime. In this thesis research, I investigated the feasibility of using *noncuring* graphene-enhanced thermal interface materials for passive thermal management of concentrated multi-junction solar cells. Using an inexpensive scalable technique, graphene and few-layer graphene fillers, with varying concentrations, were incorporated in the noncuring mineral oil matrix. The graphene filler loading of up to 40 wt% has been used. The thermal interface material was applied between the solar cell and the heat sink. The performance parameters of the solar cells were tested using an industry standard solar simulator with concentrated light illumination of up to 200× suns. For comparison, commercial thermal interface material was also tested. It was found that the noncuring graphene enhanced thermal interface material substantially improves the photovoltaic cell's open circuit voltage. The improvement is achieved via a reduction in the cell's temperature under concentrated sun. The performance of the noncuring graphene thermal

interface material was better than that of the commercial reference sample. The obtained results in this thesis are important for the development of the thermal management technologies for the next generation of photovoltaic solar cells.

# Table of Contents

# List of Figures

# List of Tables

# Chapter 1

## 1.1 Motivations

Due to increase in energy demands and depletion of non-renewable energy resources, there is an increase in research activities on efficiently harnessing energy from renewable sources like solar, wind, and nuclear energy. Solar energy is a very promising candidate for sustainable energy resource due to its clean, abundant, accessible, and affordable nature. The world's annual energy consumption is less than the amount of energy from sun reaching earth's surface over one hour of irradiation. Photovoltaic (PV) energy generation allowing for a direct energy conversion of sun power to electricity have attracted a lot of interest from both scientific and practical points of view. The first silicon solar cell was developed in 1954 at Bell Labs in the United States [1]. Although, this solar cell had an efficiency of only 6%, this marked a new era in technology advancement in non- renewable energy.

Mostly, solar cell developments aim to reduce manufacturing cost and improve power conversion efficiency (PCE) [2–4]. Currently, crystalline silicon solar cells occupy about 90% market of the commercially available solar cells and have the maximum PCE of about 26%, but the majority of the solar cell have efficiency between 12% - 16% as high efficiency solar cell are expensive [5–8]. The multi-junction solar cells with concentrators have the efficiency of more than 40%, and they are the highest efficient PV cell technology known. The remaining energy is converted into heat within the solar cell increasing its

operating temperature [9–11]. This increase in solar cell temperature will decrease PCE and will be detrimental to the lifetime of solar cells. It is found that under continuous solar irradiation, the polycrystalline and monocrystalline Si solar cells can reach temperatures of 40 °C to 65 °C leading to efficiency loss of 0.35% - 0.5% per unit K temperature rise [12–15]. It is very important to extract the excess heat from the solar cell in order to have higher power generation. Passive cooling techniques like heat sinks are used along with solar cells can reduce its operating temperature. A high thermal resistance between the back surface of the solar cell and heat sink can restrict the amount of heat transferred from the solar cell to the heat sink. This resistance to heat flow is caused due to surface imperfections, associated with air gaps between the attached surfaces. Since air is a poor conductor of heat, there is a need to replace it with a higher thermal conductivity material for improved heat transfer properties. Thermal interface materials (TIMs) can be used to improve the thermal conductivity of the interface layer, facilitating the heat transfer from the solar cell to the heat sink.

## 1.2 Working Principles of Photovoltaic Cells

A photovoltaic cell is a semiconductor device which can generate electricity directly from the sunlight using photovoltaic effect. This phenomenon was first demonstrated by Edmond Becquerel in 1839 using electrochemical cell and the first solar cell was developed using layer of selenium between thin film of gold by Charles Fritts in 1884 [16]. A conventional solar cell is fabricated by joining p-type doped and n-type doped semiconductor material together. Figure1.1 shows the schematic diagram of a single

junction solar cell. The p-type doped material has holes as majority carrier and n-type material have electrons as their majority carrier. A depletion / space-charge region is formed due to electron-hole recombination at the junction of the p-type and n-type material. Electrons from n-side diffuse into p-side and holes from p-side diffuse into n-side which develops a potential difference called as "built-in potential". At equilibrium, the junction has a band gap energy of $E_G$, which is the difference in energy between upper edge of the valence band and lower edge of the conduction band. When sunlight incidents on the p-n junction, photons with energy ($E = hv$) equal to or higher than the $E_G$ is absorbed aiding an electron-hole pair generation. This process is called photogeneration where free electron and holes are generated. The built-in potential of the p-n junction accelerates the generated free electrons towards n-side and generated free holes to drift towards p-side towards external contact. This creates a potential difference at the external contacts which can be utilized to drive current through a given external load [16].

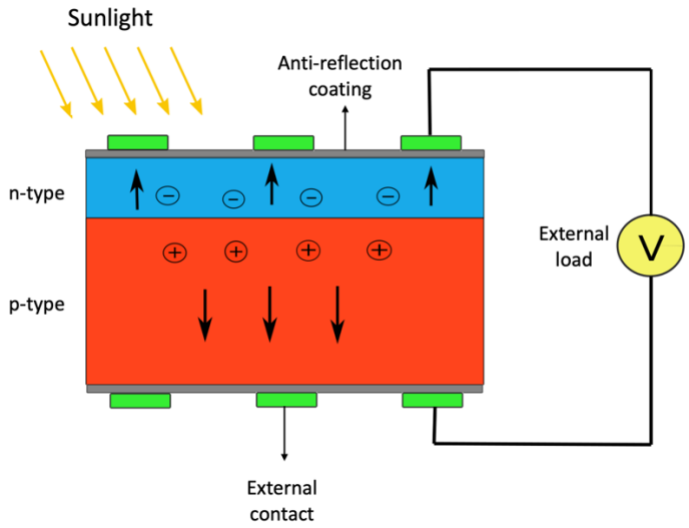


**Figure 1.1:** Schematic of a single junction solar cell.

The two major parameters used for defining photovoltaic cell characteristics are open circuit voltage ($V_{OC}$) and short circuit current ($I_{SC}$). The open circuit voltage is defined as the maximum potential difference in a solar cell when infinite resistance load is connected and zero current flow. The short circuit current is defined as the maximum current flow when the external load is zero (short circuited) and having zero voltage [16].

During a regular use of solar cell, i.e. when an external load is connected, the current flow will be less than $I_{SC}$ and the potential difference across the load will be less than $V_{OC}$ ( $I < I_{SC}$ and $V < V_{OC}$). The solar cell output power for a given temperature is as follows:

$$P = IV \tag{1.1}$$

The maximum power conditions can be calculated by differentiating equation (1.1) and equating it to zero [16]:

$$dP = d(IV) = 0 \tag{1.2}$$

The real maximum power output equals to

$$P_{mp} = I_{mp}V_{mp} \tag{1.3}$$

## 1.3 Multi-Junction Solar Cells

The theoretical power conversion efficiency limit of single junction solar cells is the main motivation for development of multijunction solar cells. In 1961, Shockley–Queisser described the efficiency limit of a single p-n junction solar cell by balancing of the radiative transfer between sun and solar cell, modeled as black bodies. They calculated the efficiency

limit to be around 31% for a 1.3 eV material at 1 sun illumination at room temperature [17].

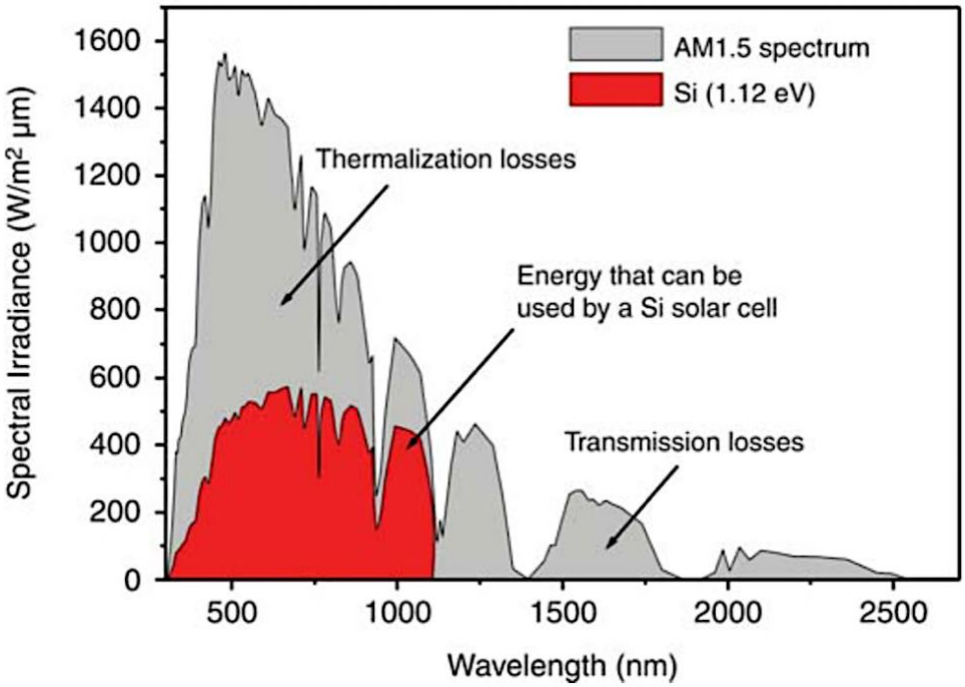


**Figure 1.2:** AM 1.5G solar spectrum and the part of the spectrum that can theoretically be used in Si solar cell. Reproduced from Dimroth, F.; Kurtz, S. High-efficiency multijunction solar cells. MRS Bulletin 2007, 32, 3, 231, with permission of Cambridge University Press. 

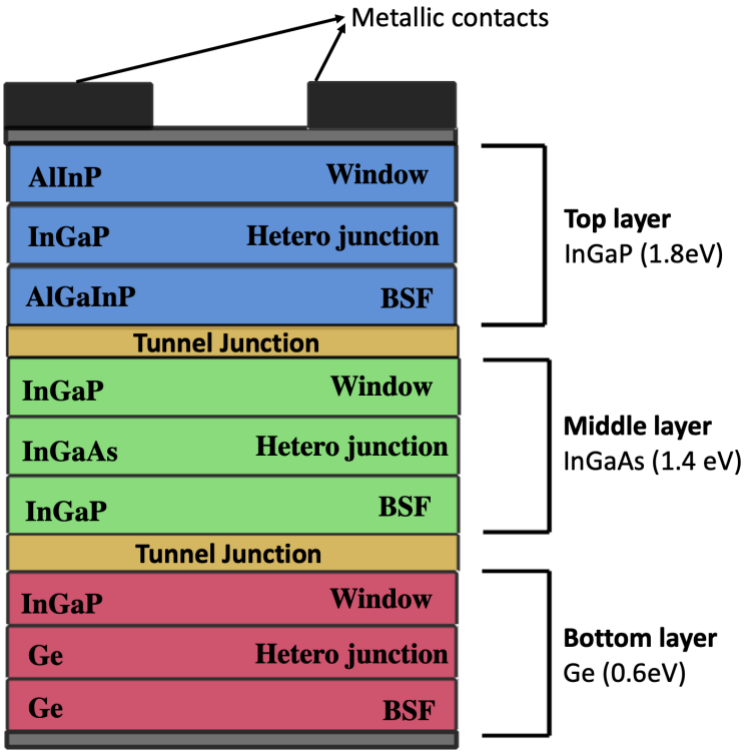


**Figure 1.3:** Schematic diagram of a triple-junction solar cell.

By stacking of different layers of material, the thermalization losses are reduced drastically compared to the single junction solar cell as high energy photons are utilized for electron-hole pair generation [18]. Also, using low bandgap energy materials as bottom layers can be used to reduce transmission losses *i.e.* low energy photons not being used for electron-hole pair generation. Though multiple layers of different band gap materials in a single solar cell might be used for increasing efficiency, but not feasible for all materials. Upon stacking layers of polycrystalline and amorphous materials can result in decreased efficiency of the solar cell. This phenomenon is observed because minority charge carriers, after drifting through the depletion region, recombine in the bulk defects and surfaces and do not contribute to power generation [19]. In order to achieve very high efficiency, higher

crystallinity of the layers play a crucial role. High crystalline material can be fabricated separately, and mechanically stacked or multiple layers grown on top of each other on a single substrate. Single crystalline multijunction solar cells have high efficiency compared to polycrystalline and amorphous multijunction solar cells. The symbols in Figure 1.4 depict the practical maximum efficiency of different crystalline solar cells and the solid lines depicts the theoretical limit for the same. The efficiency of the solar cell can be increased by improving the quality, uniformity, and crystallinity of the solar cells. We also need to consider the diffusion length of the minority charge carriers in the different layers of material. It is important to ensure that the minority charge carrier diffusion length is higher than the thickness of the material to ensure low recombination.

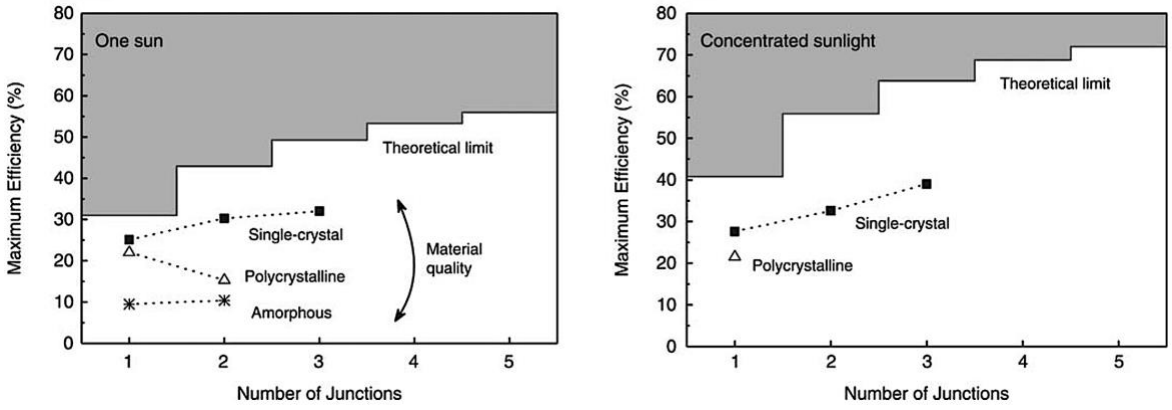


**Figure 1.4:** Practical and theoretical limit of power conversion efficiency of different crystalline solar cells under one sun and concentrated sunlight. Reproduced from Dimroth, F.; Kurtz, S. High-efficiency multijunction solar cells. MRS Bulletin 2007, *32*, 3, 231, with permission of Cambridge University Press. Copyright © 2011, Cambridge University Press.

Minority charge carrier lifetime is another factor to be considered for efficiency optimization. Although a lot of factors affect the lifetime of the minority charge carrier, the major cause for loss of lifetime is due to carrier recombination in the junctions due to

impurities, grain boundaries, and point defects. This problem has been rectified by using high quality deposition atomic layer of III-V group materials.

In order to achieve high minority charge carrier lifetime and diffusion length, it is necessary to ensure that the lattice parameters of the different layers are matched. Since mismatch in lattice parameters can induces surface defects which in turn will affect the flow of charge carriers. It is also important to mention that the different types of crystal alloys like random, ordered, quantum wells, and quantum dots affect the flow of charge carriers within the layers of solar cell [20,21]. Theoretical maximum possible efficiency has been calculated by detailed balance limit of an infinite layers p-n junction solar cell under 1 sun illumination is around 68.2% and with concentrated illumination of 45,900× suns, the efficiency reaches up to 86.8% [22]. Overall, solar cells made from stacking up of multi-layer single crystalline materials with varying bandgaps absorbs higher amount of energy from the solar spectrum compared to single junction solar cell as shown in Figure 1.5.

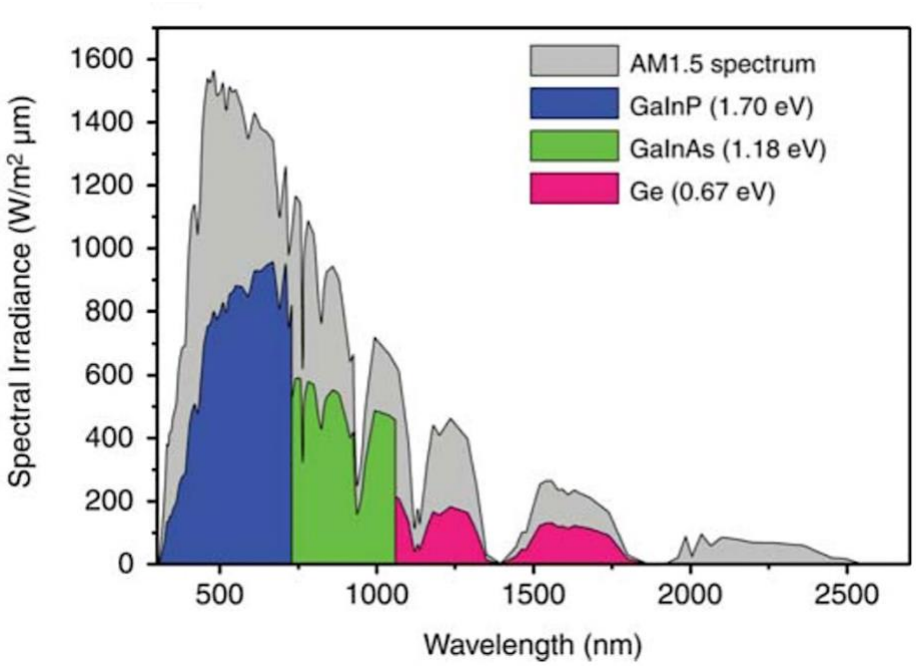


**Figure 1.5:** AM 1.5G solar spectrum and the part of the spectrum that can theoretically be used by GaInP/GaInAs/Ge cell. Reproduced from Dimroth, F.; Kurtz, S. High-efficiency multijunction solar cells. MRS Bulletin 2007, 32, 3, 231, with permission of Cambridge University Press. Copyright © 2011, Cambridge University Press.

A common triple-junction solar cell contains a top layer ($E_G$ = 1.7-1.9 eV), middle layer ($E_G$ = 1.3-1.5 eV) and, bottom layer ($E_G$ = 0.5-0.8 eV) to absorb photons with different energy ranges for electron-hole pair generation. The other major features of a multijunction solar cell structure (refer Figure 1.3) includes:

- **Window layer:** It is a layer made of high band gap material which allows most of the incident photons to pass through. It helps in reduction of surface recombination velocity and provides surface passivation. It aids in selective contact for electrons to tunnel through and holes to reflect back.
- **Back surface layer (BSF):** It is a layer made of high band gap materials which allows incident photons to pass through. Similar to window layer, it helps in reduction of

surface recombination velocity and provides surface passivation. But BSF layer aids in selective contact for holes to tunnel through but holds the electron back.

- **Tunnel junction:** It is a heavily doped p-n diode which separates two sub-cells of multijunction solar cell. Due to the very high doping along with very low depletion region, it aids in tunneling of electrons generated from the bottom layer to the top layer. This reduces the need for multiple terminals between each layer of the solar cell to extract the generated electrons which results in high $V_{OC}$.

Currently, a four-junction (AlGaInP / AlGaAs / GaAs / GaInAs) photovoltaic cell has the maximum power conversion efficiency of 47.1% at 143× suns illumination (1 sun power = 1 kW/$m_2$) [23,24]. Though multi-junction solar cells technology has been proven to be highly efficient compared to the conventional Si solar cells, thermal management of excess heat generated within the cell present a major problem [25].

## 1.4 Other Types of Solar Cells

Solar cells can be classified on the basis of various factors. Solar cells are majorly classified on the basis of the semiconductor material they are made from. Each material has unique property of absorbing light for photocurrent generation. Some are efficient for application on earth's surface while the others are for outer space. Solar cells can be made of only one layer of light absorbing material (single junction) or made of multiple layer of light absorbing material (multi-junction) for increased absorption and photocurrent generation. Solar cells can also be classified as first, second, and third generation. First generation solar

cells are the conventional crystalline Si solar cells (monocrystalline and polycrystalline) which are predominant in PV market. Second generation solar cells are CdTe thin films and copper indium gallium selenide (CIGS) cells which are majorly used in photovoltaic power stations and integrated power systems in large-scale industries. Third generation solar cells are very highly efficient and expensive which are emerging PV technologies majorly under development in research institutions [26]. The following are the major types of solar cells:

- **Crystalline silicon solar cells:** The most commonly available photovoltaic cells in the market. They can be polycrystalline or monocrystalline Si with donors and acceptors being doped to make a p-n junction. Monocrystalline solar cells are relatively expensive, but exhibit higher efficiency compared to polycrystalline solar cell.
- **Cadmium telluride solar cells:** This type of solar cell uses cadmium telluride thin film to absorb light to generate current. The only thin film technology where manufacturing cost is lesser than crystalline Si solar cell for higher kilowatt power generation [27]. They have the lesser carbon footprint compared to the Si solar cell manufacturing process. But the CdTe thin film is toxic and must be handled with care. Thus, making it inaccessible for household solar cell applications [28].
- **Perovskite solar cells:** The absorber material in this type of solar cell has $ABX_3$ crystal structure. The most commonly used absorber material for perovskite solar cells is methylammonium lead trihalide with bandgap ranging from 1.5 eV to 2.3 eV [29]. The manufacturing process is rather simple compared to that of Si solar cell which includes multistep processes and needs a clean room facility for high purity Si crystal growth.

In contrast, perovskite solar cells can be manufactured in traditional wet chemistry processing techniques like spin coating and baking [30]. Although they are cheaper to make and more environment friendly, their efficiency is lower compared to crystalline Si solar cells.

- **Dye sensitized solar cells:** These are third generation solar cells, which uses a photo sensitive anode and an electrolyte to form an electro-photochemical cell. The important features of these cells are that they are semi flexible, semi-transparent, and require simple manufacturing techniques. This makes them a viable candidate for both indoor (replacing glass in home windows) and outdoor applications. A lot of research and development is still needed to make it feasible for the different outdoor weather conditions [31]. Although, the contacts (platinum) and electrolyte are expensive, the power-to-cost ratio is relatively close to fossil fuel power generation which attracts interests from lots of European Union countries.

Other solar cell types include quantum dot solar cells, nanocrystal solar cells, copper indium gallium selenide (CIGS) solar cells, gallium arsenide germanium solar cells, micro-morph cells, photoelectrochemical cells, polymer solar cells, hybrid and biohybrid solar cells.

## 1.5 Effect of Temperature on Performance of the Solar Cells

The photons incident on the solar cell have different energies which correspond to different wavelengths. Photons with energy equal to or higher than the band gap of the solar cell is

utilized to electron-hole pair generation which leads to photocurrent generation. The excess energy of photon above the solar cell bandgap and photon of low energy will be converted to kinetic energy which will generate heat increasing the operating temperature of the solar cell. The short-circuit current density, $J_{SC}$ , open-circuit voltage, $V_{OC}$, fill factor, $FF$, and power conversion efficiency, $\eta$, are the major parameters affecting of the PV cell performance as discussed earlier in Chapter 1.2 [32].

All of these parameters change with varying temperature. Firstly, as the temperature increases the bandgap of materials decreases as we can see from Eq.1.4. The open-circuit voltage is affected by the increase in temperature majorly due to the following diode factors: ideality factor, *n*, saturation current density, $J_0$, series resistance, $R_S$, and shunt resistance, $R_{SH}$, of the solar cell. The increase in values of $R_S$, $R_{SH}$ and $J_{SC}$ is insignificant with increase in temperature, so it does not influence the efficiency of the cell much [33]. But $J_0$, a material dependent factor, which changes drastically with increase in temperature, affecting the $V_{OC}$ value and, eventually, the PV conversion efficiency [34–37].

$$E_g(T) = E_g(0) - \frac{\alpha T^2}{T+\beta} \tag{1.4}$$

$$J_0(T) = CT^3 \exp\left(-\frac{E_g}{k_B T}\right) \tag{1.5}$$

$$J = -J_{PH} + J_0(e^{qV/nk_BT} - 1) \tag{1.6}$$

Where $C$ is a constant number, $E_g$ is the bandgap of the material, $T$ is the absolute temperature of the solar cell, $k_B$ is the Boltzmann's constant, $J_{PH}$ is the photo-generated current density, and $q$ is the electron charge.

With increase in temperature, the effective bandgap of the solar cell decreases, which increases the number of photo-generated electrons. As $E_g$ decreases and temperature, $T$, increases the effective saturation current density, $J_0(T)$, also increases (see Eq. (1.5)). The current density-voltage characteristic of a p-n junction solar cell is given by Eq. (1.6). The open circuit voltage is the maximum voltage obtained from the solar cell, *i.e.*, $V_{OC}$ in Eq. (1.7) is obtained by equating $J = 0$ in the Eq. (1.6) and $J_{PH} \approx J_{SC}$ [38].

$$V_{OC}(T) = \frac{nk_BT}{q} \ln\left(\frac{J_{SC}}{J_0} + 1\right) \tag{1.7}$$

Since $J_0$ increases with increase in temperature, the effective open-circuit voltage, $V_{OC}(T)$ of the solar cell decreases drastically. The fill factor of a solar cell (FF), a measure for the squareness of the IV curve is defined as the ratio of real maximum power output ($P_{Max}$) to the ideal maximum power output (product of the $V_{OC}$ and $J_{SC}$) as shown in Eq. (1.8). Currently, the fill factor for the multi-junction solar cells ranges from 0.7 to 0.88 [39]. The efficiency of the solar cell ($\eta$) is defined as the ratio of the maximum output power to the incident irradiation ($P_{in}$) (Eq. 1.9). Since $FF$ and $J_{SC}$ do not change much with temperature, and the power of the incident irradiation is constant and $V_{OC}$ strongly decreases with temperature rise, the efficiency of the solar cell decreases with increase in temperature.

$$FF = \frac{P_{Max}}{V_{OC} \cdot J_{SC}} \tag{1.8}$$

$$\eta = \frac{P_{Max}}{P_{in}} = \frac{FF. J_{SC}. V_{OC}(T)}{P_{in}} \tag{1.9}$$

For these reasons, the temperature effects on the performance of conventional and multi-junction solar cells has been a subject of many studies [40–43]. It is very crucial to

extract the dissipated heat from the solar cell, since the increase in solar cell operating temperature, in the short term, can lead to power conversion efficiency loss and, in the long-term, degradation of the lifetime of the solar cell [25, 44–47].

## 1.6 Thermal Management of Solar cells

Most commonly used methods for extraction of heat from an electrical system are active cooling, phase change materials (PCMs) for heat storage, and passive cooling

### 1.6.1 Active Cooling

In this method of heat extraction process, external machine is needed for forced convection to extract the excess heat from the system. One of the main advantages of this method of cooling is the increased rate of flow of fluid, which facilitates better excess heat extraction. The major drawback for this method is the additional cost involved for operating the external machines [48]. The following are few active cooling methods used:

- **Forced air:** The most commonly used active cooling technique, which utilizes fans to circulate air directly over the heat source and heat sink. Due to forced air flow, the heated air is channeled out of the system through exhaust which significantly improves heat dissipation. It is mostly commonly used in desktop computers for cooling down processors and hard drives.
- **Forced liquid:** This is an active cooling method in which liquid is pumped through the system for heat extraction. A liquid coolant is pumped through a closed tube loop above

the heat source to extract the heat. Cold plates are metal structures with internal cooling channels / pipes for circulation of coolant liquids. Cold plates are used for localized heat extraction by transfer of heat to the coolant, which further flows through a heat exchanger to dissipate the heat. Cold plates are attached to the printed circuit boards (PCB) containing heat generating components.

- **Thermoelectric coolers (TEC):** These are thin layer of materials attached between heat source and heat sink. When a potential difference is applied to TEC, a temperature differential is formed which enhances the heat dissipation.

### 1.6.2 Phase Change Materials

These are materials which utilizes phase transitions to absorb and release energy from heat generating systems. These materials have high latent heat of fusion, due to which the material keeps absorbing heat when the system is heated, leading to a phase transition. The absorbed energy is released back to the system during the cooling cycle [49]. Phase change materials are chosen according to the operating temperature of the system. The phase transition temperature of the PCMs should be close to the maximum operating temperature in order to achieve maximum heat extraction, since PCMs use the latent heat of fusion for heat dissipation from the heat source [50–53]. PCMs are one of the most commonly available method for heat extraction. They are very inexpensive, non-toxic, non-corrosive, chemically stable, highly durable, and reliable. One major disadvantage is that very less heat is extracted from the system using PCMs [53]. Another notable disadvantage is the supercooling effect in salt hydrate PCMs which will interfere the heat extraction drastically

[54]. They are one of the preferred cooling techniques in PV technologies due to their abundance and less cost [55]. Using PCMs in solar cell can reduce the rise in temperature of the solar cell by up to $20^0$-$25^0$C compared to when no PCMs being used [56,57].

## 1.6.3 Passive Cooling Techniques

It is a cooling technique which relies solely on the natural convection and no external energy for heat dissipation. They are highly reliable, inexpensive, and easiest to implement [58–60]. Some of the major passive cooling techniques are as follows:

- **Heat sinks:** It is the most commonly used passive cooling technique. They are made from high thermal conductivity material like aluminum and copper which are mounted to the heat source. They are generally a flat panel with different designs of fin-like structures on one side while the other side is flat and attached to the heat source. Natural convection occurs as the heat is transferred from the heat source to the heat sink and dissipated from the fins on the other side. This has application ranging from small electronics to huge turbine generators.
- **Heat pipes:** This is one of the most efficient heat extraction technique. It consists of a sealed, hollow tube containing a liquid coolant. One end of the tube is attached to the heat source and the other end is attached to a heat exchanger like heat sink. They are high thermal conductivity metals like copper which can be flat or bent shape depending of the application. Most common application of heat pipes are laptops.

- **Heat spreader:** These are highly thermal conductive metal plates which are used to distribute the heat evenly from a concentrated heat source. They are often mounted as back plates to PCB with heat generating components.

## 1.7 Thermal Interface Materials (TIMs)

A high thermal resistance due to the airgap in between the back surface of the heat source and heat sink can limit the amount of heat transferred. Thermal interface materials are polymeric based materials used to enhance the heat dissipation between the two surfaces. TIMs are generally in the form of paste which fills and replaces the airgaps and provide a better thermal contact between the surfaces. The heat transfer capability of the TIMs depends on the thermal conductivity values of the TIMs. High thermal conductivity TIMs provide better heat dissipation and thermal contact between the surfaces [59–65]. Commercial TIMs are made of high thermal conductivity metallics and ceramic fillers along with polymeric base material for better electrical insulation to enhances heat extraction [66]. The reliability and durability of TIMs are important factors to be considered. Applications with long operating time needs TIMs with higher viscosity and base material with higher glass transition temperature in order ensure minimum leakage and degradation of TIM [67].

The thermal resistance ($R_{TIM}$) for the interface layer between two surfaces depends on the distance between two layers *i.e.* bond layer thickness (BLT) and contact resistance ($R_{C1}, R_{C2}$) of both the surfaces. This can be calculated as follows [68–70]:

$$R_{TIM} = \frac{BLT}{K_{TIM}} + R_{C1} + R_{C2} \quad (1.12)$$

where $K_{TIM}$ is the thermal conductivity of the TIM.

It can be inferred that higher thermal conductive TIMs, lower contact resistance and lower BLT can reduce the overall thermal resistance of the interfacial layer.

## 1.8 Graphene as Fillers for TIMs

Graphene, an allotrope of carbon with single layer of carbon atoms, exhibits exceptional intrinsic thermal conductivity values of up to ~5000 W/mK in-plane depending on the size and quality [71–76]. Graphene shows very high electron mobility and very low resistivity values. The ongoing research in electronics industry focuses on development of smaller and highly capable processors and memory storage devices [77]. This leads to high power density devices which can heat up rapidly demanding better heat dissipation. Commercial TIMs use silver or aluminum particles with very high loading fractions to achieve higher thermal conductivity. But high loading fraction of fillers can increase production cost. Graphene also exhibits very high compatibility with polymers which are used as base materials for TIMs. For these reasons, graphene can be used as fillers in the polymer matrices which drastically increases the thermal conductivity of the TIMs [78–84]. It has been verified that decreasing the lateral dimension of the graphene layers reduces its thermal conductivity. Therefore, graphene flakes with micrometer-scale lateral dimensions are preferred over graphene nanoparticles for thermal management applications [69]. In the thermal context, mixture of graphene and FLG flakes can be

referred as “graphene fillers”. While the intrinsic thermal conductivity of FLG is lower than that of single layer graphene, FLG fillers have the advantages of a larger cross-section for heat transfer. Optimization of the size and thickness of graphene fillers can lead to further improvements in thermal management applications [78–81,85,86].

# Chapter 2

## 2.1 Experimental Setup

This chapter describes the instruments and methodologies used for preparing TIMs and testing multijunction solar cells with TIMs applied on, for solar cell performance characteristics. For this research, industry standard solar simulator from Newport Corporation was used to simulate sunlight for testing the solar cells. In order to measure the thermal conductivity of the TIMs used for experiments, TIM tester from Longwin was used. Kinematic viscometer from Cannon Instruments was used to measure the viscosity of the base material. A detailed description of each equipment and its working principles are given below.

### 2.1.1 Solar Simulator

Oriel Sol1A class ABA solar simulator is a very high end industrial solar simulator which complies with ASTM E927-10 (2015) standards for solar cell testing. It uses an ozone free xenon short arc lamp to generate a beam of 6”x6” beam size of 1 sun power (~ 1000 W/$m_2$). It uses a regulated high-power supply which helps ensuring uniformity in the light produced. The output power of the solar cell can be varied from 0.3-1 sun power by varying input power values. The interior of the solar simulator is insulated and generates a 5800 K black body like spectrum. The light emitted by the xenon lamp passes through multiple correction filters to produce a light beam complying with standard AM1.5G solar spectrum.

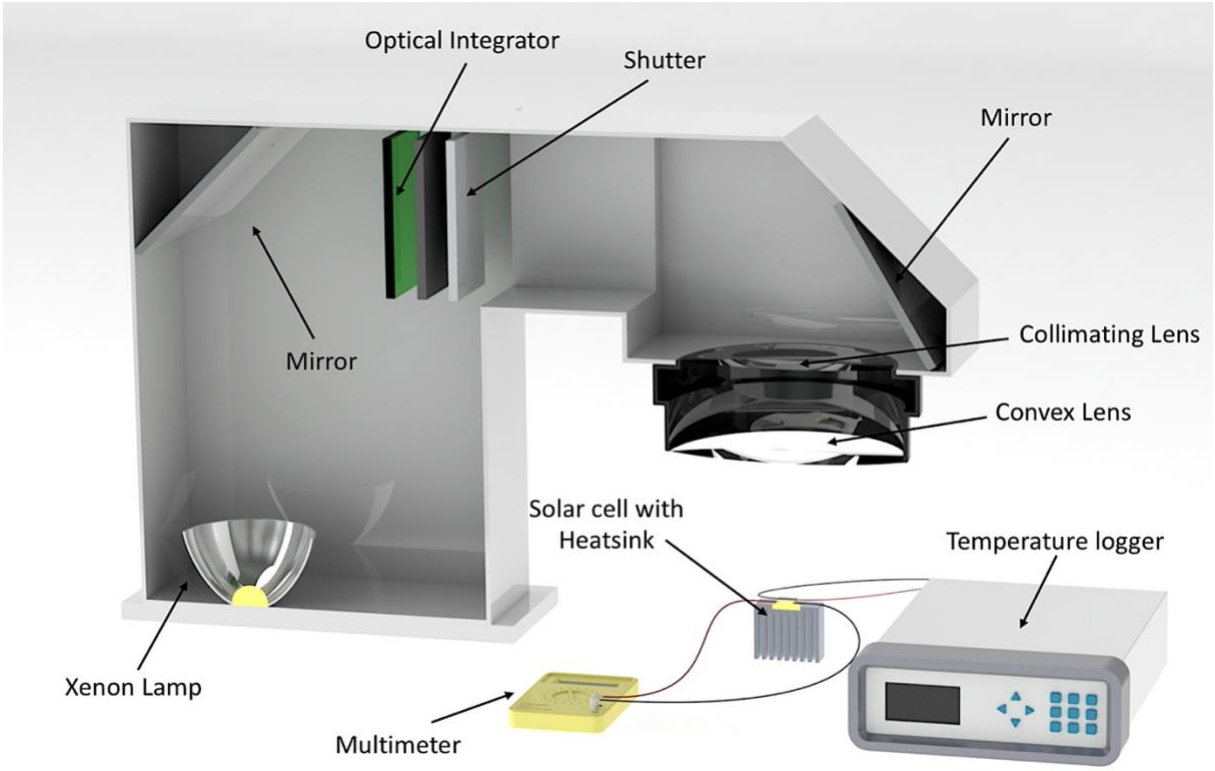


**Figure 2.1:** Schematic diagram of a solar simulator.

### 2.1.1.1 Solar Irradiation and Air Mass

Solar irradiation is defined as the total amount of power received by earth from the sun. The solar irradiance reaching earth outside atmosphere is around 1360 W/m2. As the sunlight enters the atmosphere, it loses energy due to scattering. Also, sunlight reaches the surface at various angles throughout the day, varies over different seasons and different location as well. The longer the sunlight travels in atmosphere, greater the scattering and greater the loss of energy. In order to consider all these affects, air mass coefficient was introduced. Air mass is defined as the ratio of the actual optical path of sunlight through

atmosphere to the pathlength vertically upwards at zenith. This can be expressed as AM=1/cos(θ), where θ is the zenith angle. For all mid latitudes regions on Earth which includes North America, Asia, Europe and Africa consider AM 1.5 ($\theta = 48.2_0$) as standard for representing sunlight reaching throughout the year. AM1.5G (Global) is referred as global radiation which includes direct and scattered radiation, measuring around 1000 $W/m_2$ (1 sun power). Direct radiation refers to the non-reflected, non-scattered radiation directly from sun to the collector. AM 1.5D (Direct) measures to 760 $W/m_2$ as shown in Figure 2.2 [87,88]. Scattered radiation refers to the reflected radiation from the ground reaching to the collector.

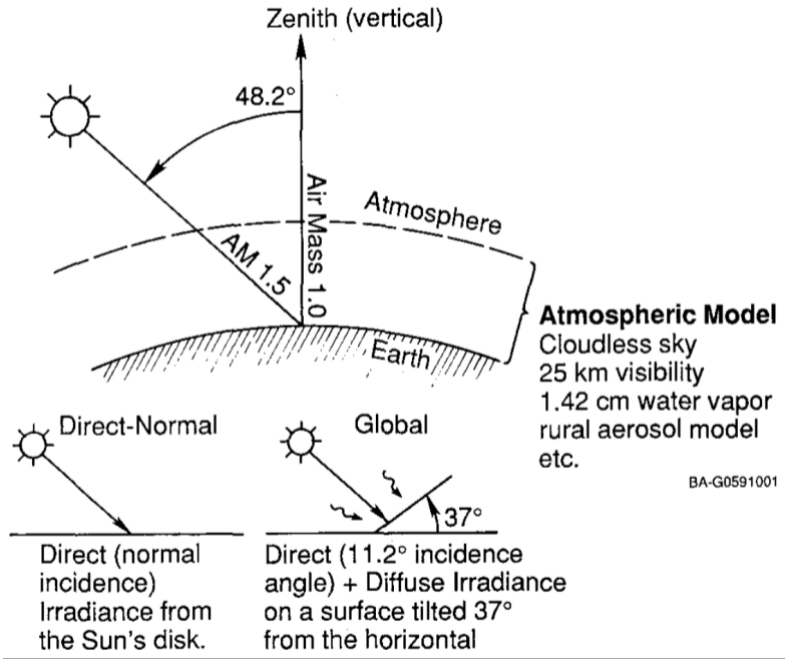


**Figure 2.2:** Schematic diagram for Air Mass 1.5 Global and Direct coefficient. Reproduced from Riordan, C.; Hulstrom, R. What is an Air Mass 1.5 Spectrum? IEEE Photovoltaic Specialists Conference, Kissimmee, FL, USA 1990, 2, 1085-1088, with permission of IEEE. Copyright © 1990, IEEE.

### 2.1.2 Thermal Conductivity Measurements of TIMs

LW-9389 TIM Thermal Interface Material Tester from Longwin North America Laboratory is a software-controlled instrument used to measure the thermal conductivity of thermal interface materials. The instrument complies with ASTM D5470-06 standard for thermal conductivity measurements. It can measure cross-plane thermal resistance and thermal conductivity along the z-axis of the sample. The TIM sample is applied between two surfaces with a temperature differential and the amount of heat transfer through the sample is calculated using Fourier's law of heat transfer. The instrument's software calculates the thermal impedance. Thermal conductivity can be extracted by calculating the product of thickness of the sample and inverse of thermal impedance. Further, thermal contact resistance can be calculated by measuring the thermal conductivity values for varying thickness and extrapolating the data for zero BLT. All the data are calculated directly from the software. This instrument can be used for thermal conductivity measurements at elevated temperatures at different applied pressure of wide range of samples like thermal greases, phase change materials, thermal tapes, gap filler pads, and graphite sheets [89]. It can also be used for long-term reliability test of the TIMs.


**Figure 2.3:** Actual image of Longwin TIM tester.

### 2.1.3 Viscometer

SimpleVIS® automated kinematic viscometer from Cannon Instruments is a single sample, portable viscometer as shown in Figure 2.4. It complies with ASTM D7279 and ASTM D445 standard for kinematic viscosity measurement of liquids. This instrument can be used to measure viscosity value ranging from 10 mm²/s (cSt) to 700 mm²/s (cSt) at 40 °C and 5.5 mm²/s (cSt) to 200 mm²/s (cSt) at 100 °C. This instrument is very portable and only needs a small quantity of sample to measure kinematic viscosity values. This instrument can be used for measuring kinematic viscosity of mineral oils, synthetic oils and formulated motor/gear oils [90].


**Figure 2.4:** Actual image of SimpleVIS kinematic viscometer.

## 2.2 Material Systems

### 2.2.1 Solar Cell

For the experiments, high efficiency GaInP/GaInAs/Ge on Ge substrate triple junction solar cells (AZUR Space (Cell type: 3C42C – 10x10 $mm^2$) were used. These cells generate an open circuit voltage ($V_{OC}$) of 3.07 V and short circuit current ($I_{SC}$) of 3.47 A at 250× suns illumination according to the technical data [91].

### 2.2.2 Graphene Fillers

xGnP® Graphene (H25) fillers from XG-Sciences with an average thickness of up to 15 nm and lateral dimension of 25 μm are used for the experiments. The graphene powder as

shown in Figure 2.6 is 99% pure, with a typical surface area of 50 $m^2/g$ to 80 $m^2/g$ and density of 2.2 $g/cm^3$ [92].

**Figure 2.5:** Graphene powder used for TIM preparation.

### 2.2.3 Commercial TIM and Mineral Oil

For this research, commonly used mineral oil (Walgreens) was used as the base polymer for graphene-filled TIM preparation. Commercially available TIM (Ice Fusion, Cooler Master Technology Inc.) was used for comparative study. It is a noncured TIM with thermal conductivity value of around 1W/mK.

## 2.3 Experimental Procedure

### 2.3.1 TIM Preparation

The noncured TIMs were prepared by homogenous mixing of mineral oil with graphene fillers, following the steps shown in Figure 2.6. The pre-determined amounts of graphene

were measured in order to synthesis 10 wt%, 20 wt%, 40 wt% mixtures in mineral oil samples. The weight percentage of graphene needed to be mixed with mineral oil was calculated as $f_g = W_g/(W_M + W_g)$, where $W_g$ and $W_M$ are the weights of graphene fillers and mineral oil, respectively. It was then added to around 30 ml of acetone to create a uniform suspension. The acetone – graphene mixture was used to avoid possible agglomeration of graphene fillers in mineral oil if otherwise added directly. The samples were sheer mixed at a low rate (310 RPM) for 20 minutes, to retain the lateral dimensions of the flakes. Following the sheer mixing, the graphene mineral oil slurries were decanted at 70°C for 2 hours, removing the excess acetone with a graphene-enhanced TIM remaining.

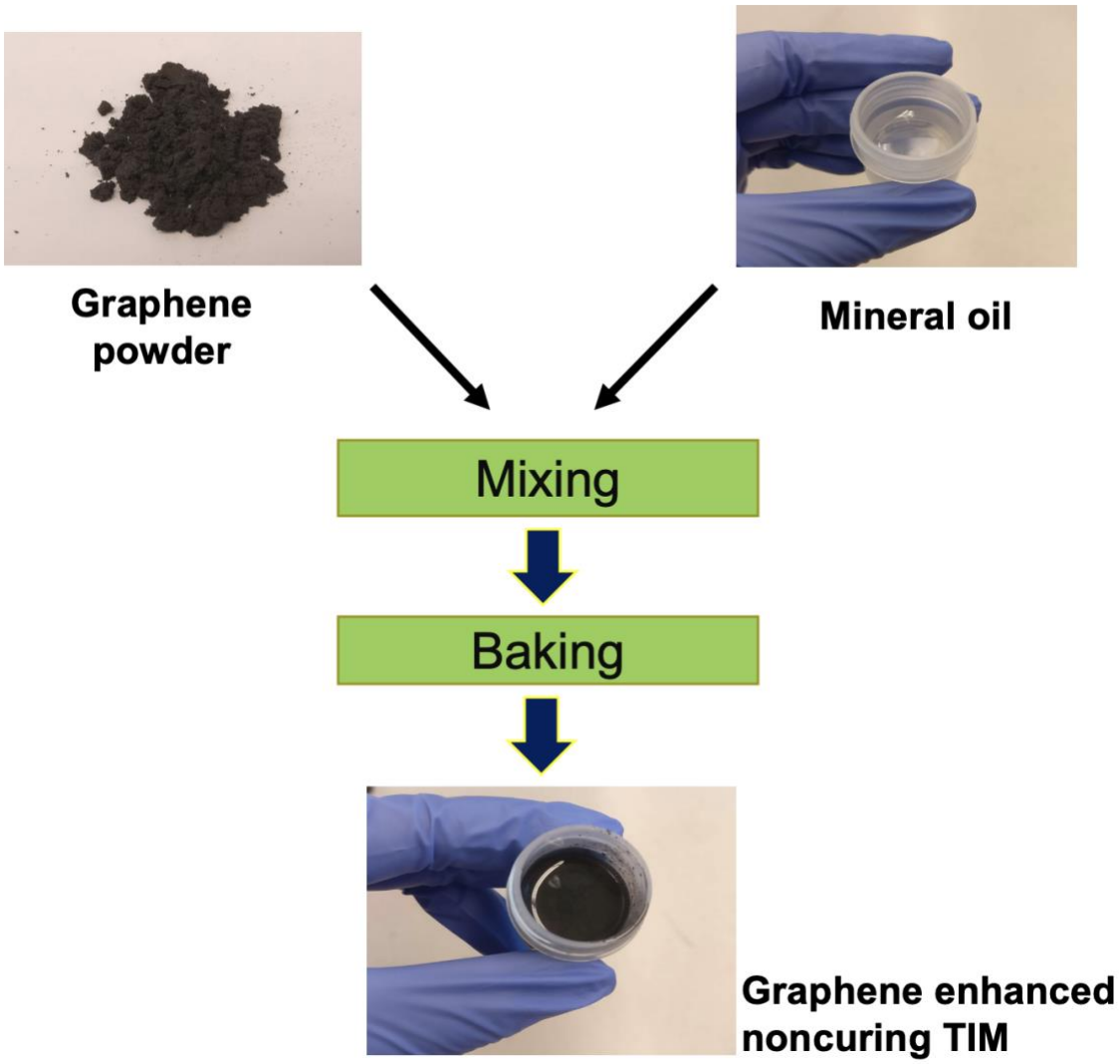


**Figure 2.6:** Flow chart of TIM preparation process.

### 2.3.2 Solar Cell Testing

The multijunction solar cell's back surface was cleaned using acetone. The TIM layer was then applied uniformly. In order to maintain a constant bond layer thickness, plastic shims of 54 μm thickness were used at the edge of the solar cells as shown in Figure 2.7.

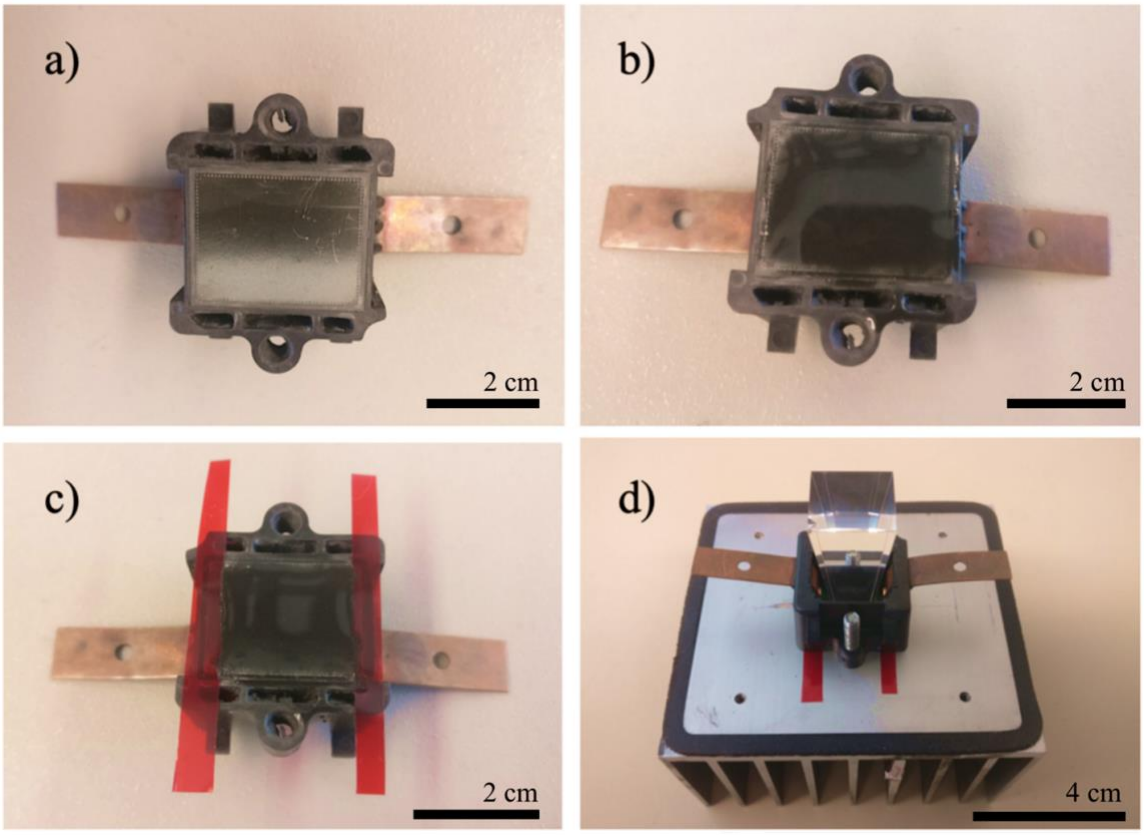


**Figure 2.7:** a) Solar cell cleaned with acetone, b) TIM uniformly applied on the back surface, c) shims attached to the edges of solar cell, and d) solar cell bolted to the heat sink with SOE on top. Reprinted with permission from Mahadevan, B.K; Naghibi, S.; Kargar, F.; Balandin, A.; Non-Curing Thermal Interface Materials with Graphene Fillers for Thermal Management of Concentrated Photovoltaic Solar Cells, C-Journal of Carbon Research, volume 6, p2, 2019.

Solar cell applied with TIM and shims attached was then bolted to the heat sink with a thermocouple attached at the bottom of the solar cell. Aluminum heat sink manufactured by extrusion with dimensions of 90 × 95 × 50 mm was used. The multi-junction solar cell with various TIMs was tested using a solar simulator (Newport, Sol1A Class ABA). A convex lens was used for converging the 1 sun power from 6”x6” beam on to the 1 $cm_2$ multi-junction solar cell which helps achieving magnification up to 200× as

shown in the Figure 2.8. The distance between the solar cell and lens was changed in order to achieve the optimum illuminations on the solar cell. Additional secondary optical elements (SOEs), like truncated square prism glass, were used to focus and direct the light on the multi-junction solar cell.

In order to achieve varying sun power, the whole setup is fixed and the Xe lamp power supply is varied from 350 W to 1000 W to achieve solar irradiation from 70× suns to 200× suns. Once the multi-junction solar cell is illuminated by the solar simulator, the open circuit voltage was measured by a multi-meter (Fluke 287) by attaching probes to the multijunction solar cell. The time-transient temperature of the solar cell was measured using a multichannel temperature logger (Applent Instruments AT4516) every 5 seconds for 30 minutes until the solar cell reached the steady state temperature condition. Figure 2.9 shows an actual image of the experimental setup.

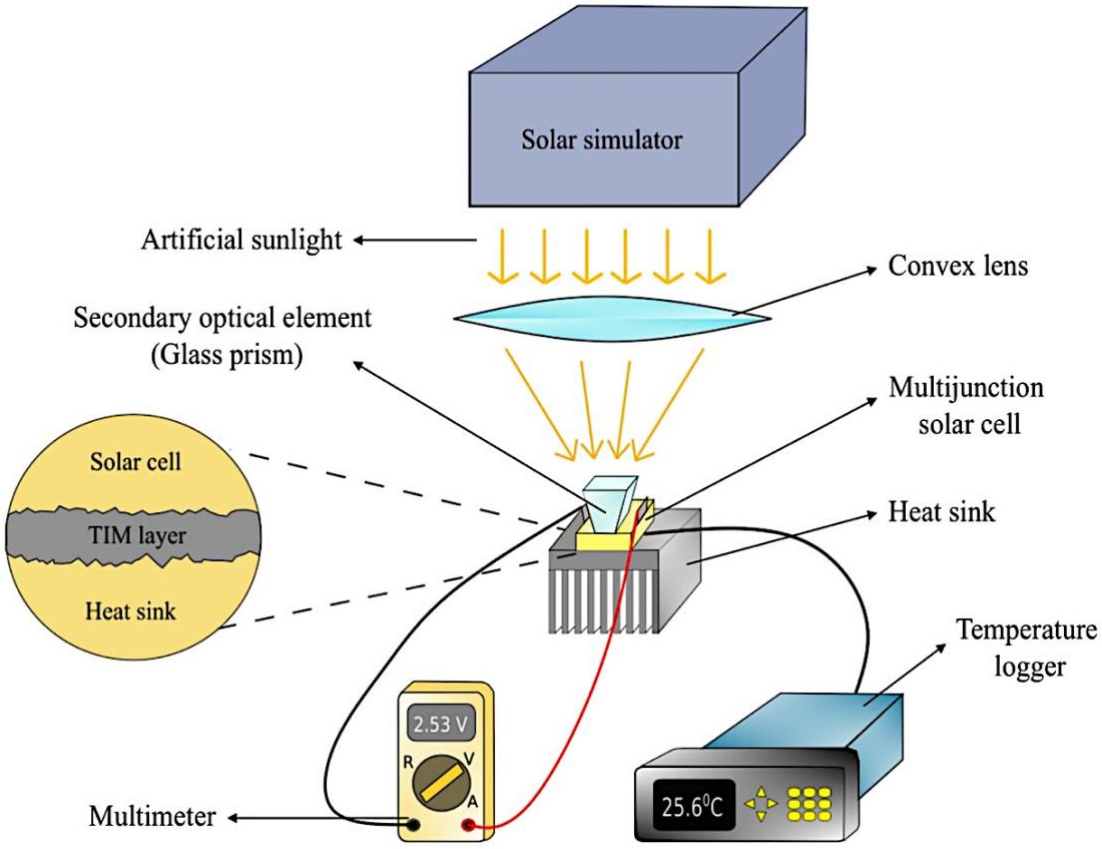


**Figure 2.8:** Schematic diagram of solar cell experiment setup. Reprinted with permission from Mahadevan, B.K; Naghibi, S.; Kargar, F.; Balandin, A.; Non-Curing Thermal Interface Materials with Graphene Fillers for Thermal Management of Concentrated Photovoltaic Solar Cells, C-Journal of Carbon Research, volume 6, p2, 2019.


**Figure 2.9:** Actual image of the solar cell experimental setup. Reprinted with permission from Mahadevan, B.K; Naghibi, S.; Kargar, F.; Balandin, A.; Non-Curing Thermal Interface Materials with Graphene Fillers for Thermal Management of Concentrated Photovoltaic Solar Cells, C-Journal of Carbon Research, volume 6, p2, 2019.

# Chapter 3

## 3.1 Overview

Thermal management of solar cells have been an interest for numerous research studies [93–95]. In our prior research, commercial TIMs with addition of low concentration of graphene were tested with solar cells [96]. The composition of commercial TIMs was not known. In this thesis research, noncuring TIMs based on mineral oil with high concentration of graphene fillers produced in-house, has been used. The limitation of the earlier work was that the high concentration of graphene fillers could not have been achieved in commercial TIMs owing to their higher viscosity. The pure mineral oil can be used to reach graphene loadings of 40 wt% which can result in better heat dissipation characteristics. Even higher loadings (>40 wt%) is possible, but not practical since excessive graphene loading can result in formation of air gaps, agglomeration of graphene fillers, and uneven dispersion of the fillers.

All TIMs were characterized for thermal conductivity and viscosity of the mineral oil was measured. In-house noncured TIMs loaded with varying graphene concentration up to 40 wt% and commercial TIM were applied between the solar cell and heat sink and tested at room temperature. The effect of rise in temperature of solar cell on open circuit voltage ($V_{OC}$) and short circuit current ($I_{SC}$) were observed for different concentration of graphene in TIMs.

## 3.2 Results and Discussions

### 3.2.1 Thermal Conductivity Measurements of TIMs

The thermal conductivity of the resulting noncuring mineral-oil based TIMs with graphene fillers was measured using TIM tester (Long Win North America Laboratory TIM Tester). During the measurements, the TIM layer thickness and temperature were carefully controlled by the TIM tester software. The thermal resistance of each sample was measured at room temperature at different thicknesses and its bulk thermal conductivity was extracted. Table 3.1 shows the results of thermal conductivity measurements of noncuring TIMs with varying concentrations of graphene fillers and a reference commercial TIM (Ice Fusion, Cooler Master Technology Inc.). It was observed that an increase in graphene concentration resulted in higher thermal conductivity values. Thermal conductivity of 6.74 W/mK was measured for the mineral oil-based TIM with 40 wt% graphene filler loading. For comparison, the thermal conductivity of the commercial TIM was only 1.34 W/mK. Upon addition of only 10 wt% of graphene to mineral oil resulted in TIM with a higher thermal conductivity than that of measured for the commercial TIM. The thermal conductivity of mineral oil with 40 wt% graphene fillers reveled the thermal conductivity of ~5 times more than that of the commercial TIM.

**Table 3.1:** Thermal conductivity of graphene-enhanced TIMs. Reprinted with permission from Mahadevan, B.K; Naghibi, S.; Kargar, F.; Balandin, A.; Non-Curing Thermal Interface Materials with Graphene Fillers for Thermal Management of Concentrated Photovoltaic Solar Cells, C-Journal of Carbon Research, volume 6, p2, 2019.

| Sample | Bulk Thermal Conductivity (W/mK) |
|---|---|
| Mineral oil | 0.27 |
| Mineral oil with 10 wt% graphene | 3.05 |
| Mineral oil with 20 wt% graphene | 4.82 |
| Mineral oil with 30 wt% graphene | 5.51 |
| Mineral oil with 40 wt% graphene | 6.74 |
| Commercial TIM (Ice Fusion) | 1.34 |

### 3.2.2 Scanning Electron Microscopy Analysis of Graphene and Viscosity Measurement of Mineral Oil

Scanning electron microscopy (TESCAN Vega 3 SEM) imaging was done to confirm the lateral dimension of the commercial graphene used for TIMs as shown in Figure 3.1. The lateral dimension of the graphene is around 20 - 25 μm which matches with the product specification data. The kinematic viscosity (SimpleVIS® kinematic viscometer) of the mineral oil was measured to be 66.3 $mm^2/s$ (cSt) at 40 $^0C$.

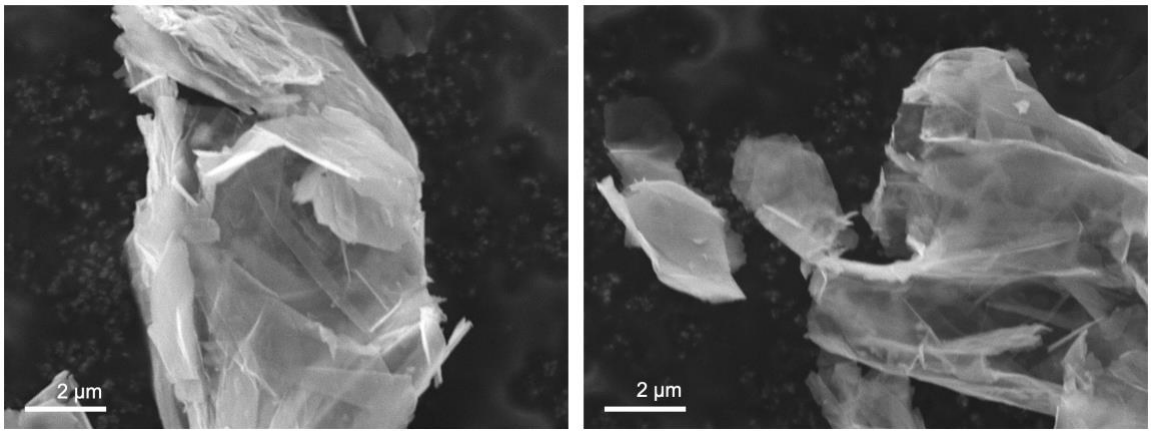


**Figure 3.1:** Scanning electron microscopy image of graphene fillers at 20kx magnification.

### 3.2.3 Short Circuit Current Measurements

The black curve in Figure 3.2 shows the short-circuit current corresponding to the illuminations of $I_1 = 70\times$ suns for the PV cell attached to the heat sink with the graphene enhanced TIM of 40 wt% filler loading. As the distance between the solar cell and the focusing lens changes slightly, some portion of the focused light falls off the inlet aperture of the SOE and hence, the illumination on top surface of the cell decreases. The blue and red curves in Figure 3.2 demonstrates the $I_{SC}$ for smaller illuminations of $I_3 < I_2 < I_1$. As expected, the short-circuit current is larger for the optimum concentrated illumination. The inset in Figure 3.2 depicts the variation of the $I_{SC}$ with time at 70x irradiation. It was observed that a little increase in the $I_{SC}$ values with time, *i.e.* increase in temperature. The increase in $I_{SC}$ is very insignificant, and it does not lead to any observable change in the efficiency of the solar cell. These experimental observations are in line with the theory described in Chapter 1.5.

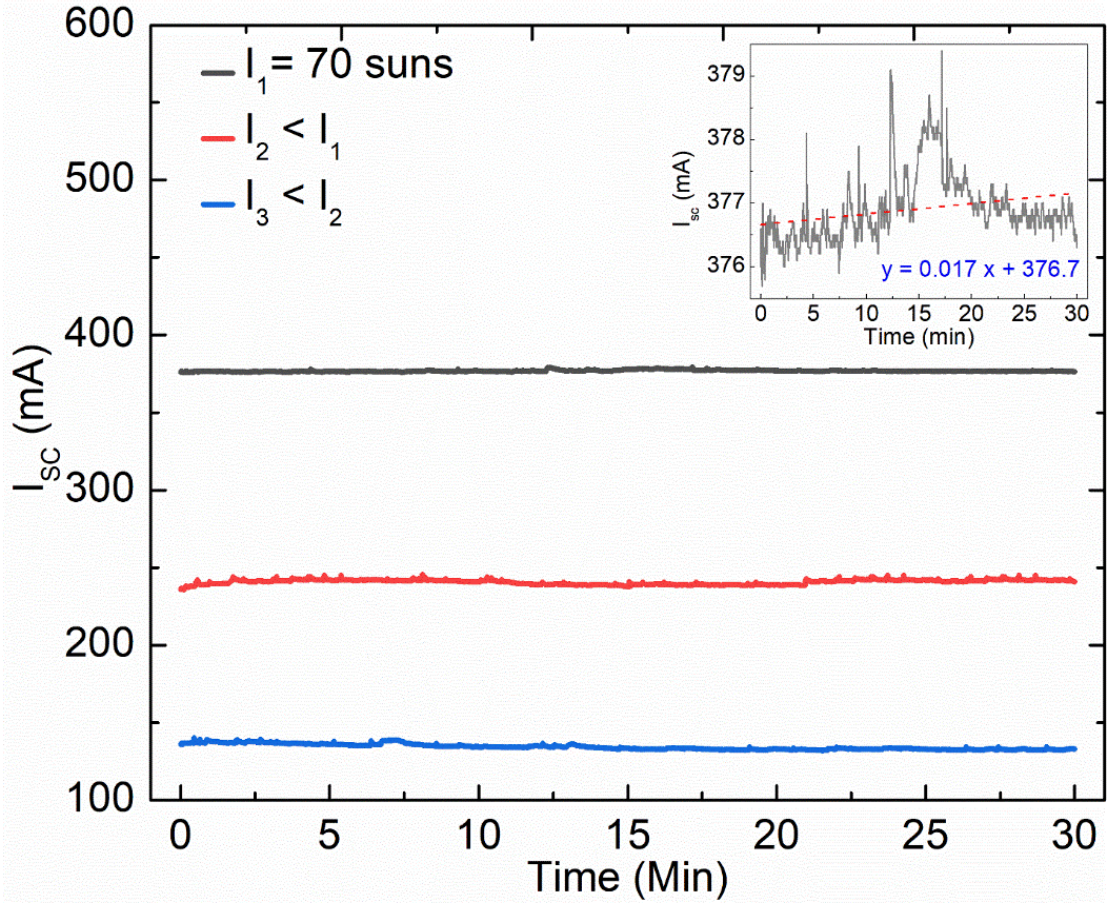


**Figure 3.2:** Short-circuit current of a solar cell as a function of time for the varying illumination up to 70× suns. The data are shown for the solar cell connected to the heat sink with noncuring TIM with 40 wt% of graphene fillers. Reprinted with permission from Mahadevan, B.K; Naghibi, S.; Kargar, F.; Balandin, A.; Non-Curing Thermal Interface Materials with Graphene Fillers for Thermal Management of Concentrated Photovoltaic Solar Cells, C-Journal of Carbon Research, volume 6, p2, 2019.

### 3.2.4 Open Circuit Voltage Measurements

The open-circuit voltage of the concentrated PV solar cells attached to the heat sink with different TIMs under fixed concentrated light illumination of 70× and 200× suns were measured. As predicted by the theory in Chapter 1.5, the major contribution to the power

loss in the solar cell was due to the decrease in $V_{OC}$. Figure 3.3 and 3.4 shows the open-circuit voltage as a function of the time. It was observed that $V_{OC}$ rapidly decreases and then saturates, as the solar cell reaches to the steady state condition, in all examined cases. The decrease in the open-circuit voltage is the largest in case of the solar cell attached to the heat sink with the mineral oil base material for both 70× suns and 200× suns illumination. The use of commercial noncured TIM allows one to improve the performance. However, there is a major improvement in the solar cell performance when the in-house noncured TIMs with graphene fillers are utilized. Table 3.2 shows the change in $V_{OC}$ values for 70× suns and 200× suns using different TIMs respectively.

**Table 3.2:** Decrease in $V_{OC}$ values while using different TIMs under 70× suns and 200× suns illumination.

| Sample | $\Delta V_{OC}$ (70× suns) | $\Delta V_{OC}$ (200× suns) |
|---|---|---|
| Mineral oil | 0.14 V | 0.85 V |
| Mineral oil with 10 wt% graphene | 0.11 V | 0.54 V |
| Mineral oil with 20 wt% graphene | 0.09 V | 0.42 V |
| Mineral oil with 40 wt% graphene | 0.08 V | 0.33 V |
| Commercial TIM (Ice Fusion) | 0.12 V | 0.62 V |

A maximum improvement of 24% reduction in decrease in $V_{OC}$ values of the PV solar cells when 40 wt% graphene fillers in mineral oil was used as compared to commercial TIM at the saturated state after 30 minutes of 70× suns illumination as shown in Figure 3.3. Similarly, an improvement of 44% reduction in decrease in $V_{OC}$ values of the PV solar cells was observed when 40 wt% graphene fillers in mineral oil was used as

compared to commercial TIM at the saturated state after 20 minutes of 200× suns illumination as shown in Figure 3.4.

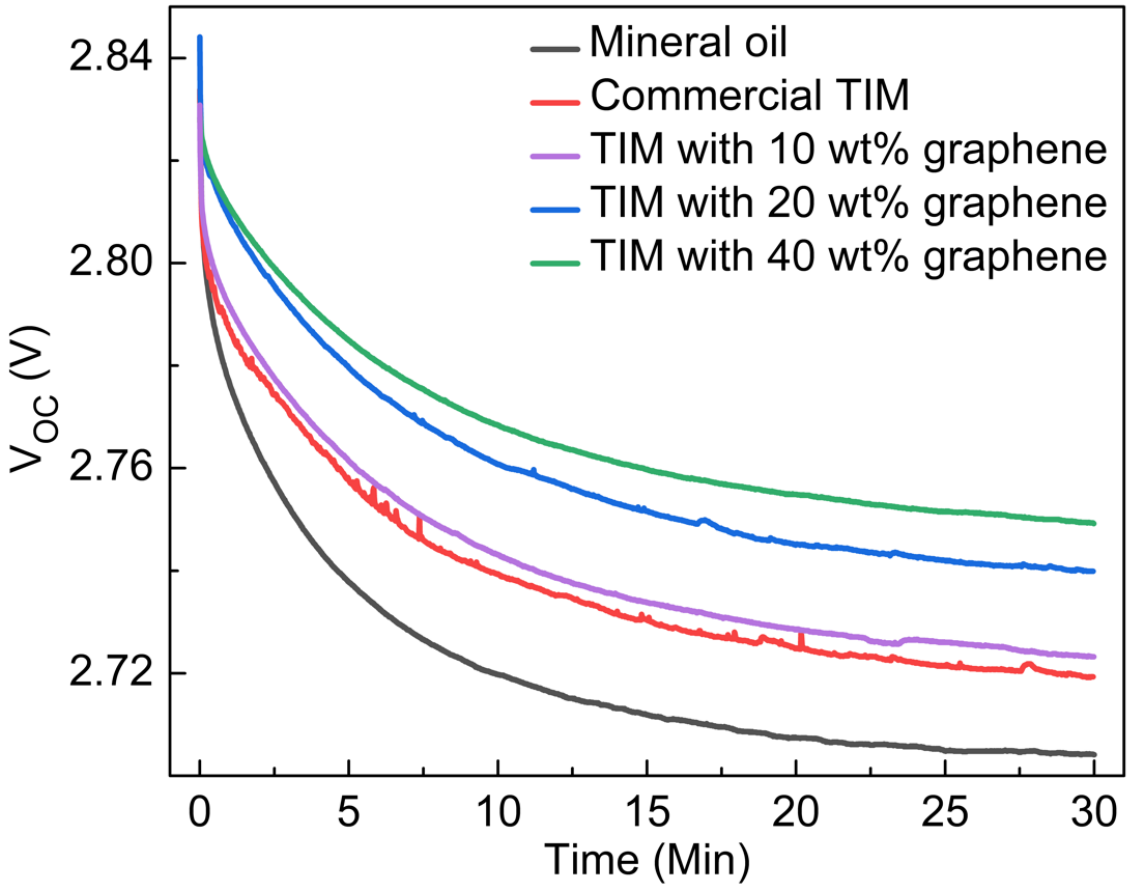


**Figure 3.3:** Open-circuit voltage of a solar cell as a function of time under constant illumination of 70× suns. Reprinted with permission from Mahadevan, B.K; Naghibi, S.; Kargar, F.; Balandin, A.; Non-Curing Thermal Interface Materials with Graphene Fillers for Thermal Management of Concentrated Photovoltaic Solar Cells, C-Journal of Carbon Research, volume 6, p2, 2019.

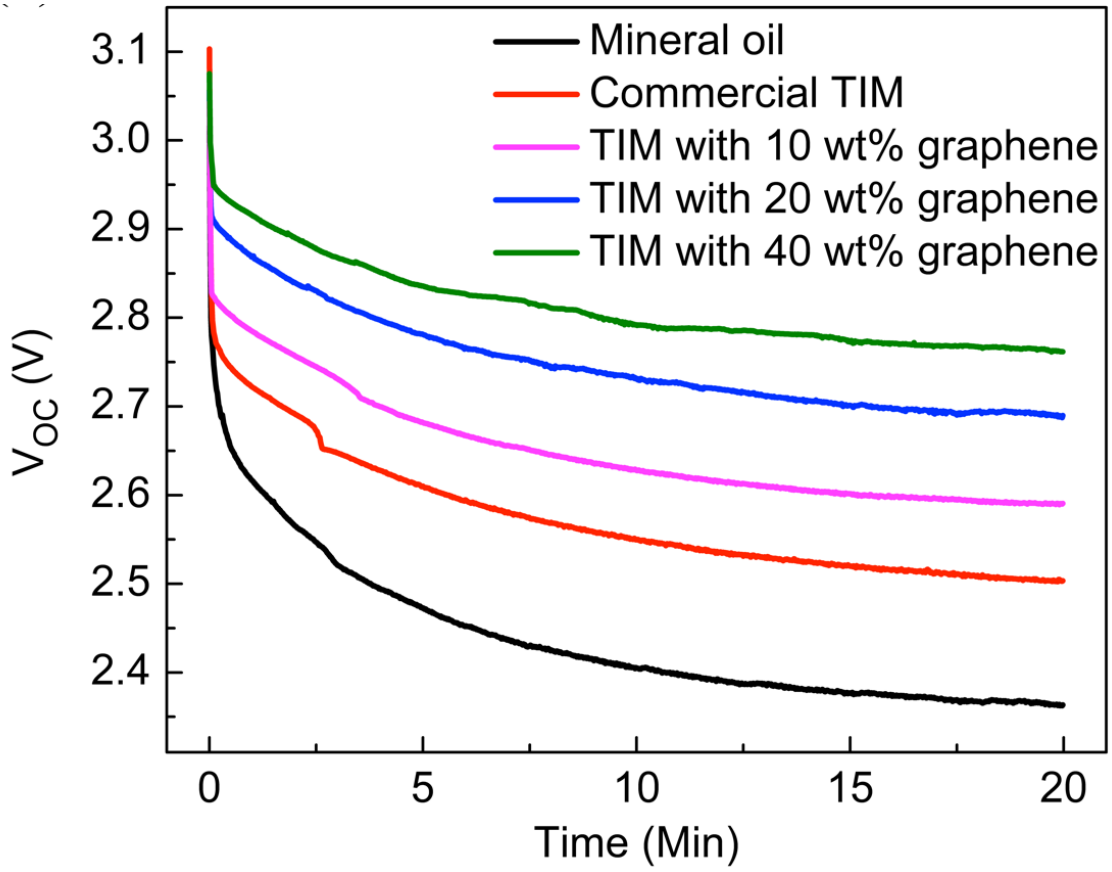


**Figure 3.4:** Open-circuit voltage of a solar cell as a function of time under constant illumination of 200× suns. Reprinted with permission from Mahadevan, B.K; Naghibi, S.; Kargar, F.; Balandin, A.; Non-Curing Thermal Interface Materials with Graphene Fillers for Thermal Management of Concentrated Photovoltaic Solar Cells, C-Journal of Carbon Research, volume 6, p2, 2019.

### 3.2.5 Temperature Rise Measurements

The rise in temperature of the PV solar cells attached to the heat sink with different TIMs at 70× and 200× suns illuminations were measured. The measurement of temperature of the solar cell complements the measurement of the thermal conductivity, *i.e.* the lower thermal conductivity of TIM results in higher solar cell temperature due to worse heat transfer from the solar cell to the heat sink. The results of the temperature rise

measurements at 70× suns and 200× suns are presented in the Table 3.3. The temperature rise in the solar cell was reduced by 31% using the noncured graphene-enhanced TIM with 40 wt% graphene loading as compared to that of the commercial noncured TIM under 70× suns illumination. The solar cell temperature increased from 25 ºC to 41.2 ºC when the commercial TIM was applied. A temperature increase of ~11 ºC, from 25 ºC to 36.3 ºC, was recorded when the noncured TIMs with 40 wt% graphene was used (See Figure 3.5).

**Table 3.3:** Increase in solar cell temperature while using different TIMs under 70× suns and 200× suns illumination.

| **Sample** | **ΔT (70× suns)** | **ΔT (200× suns)** |
|---|---|---|
| Mineral oil | 18.6 | 71.2 |
| Mineral oil with 10 wt% graphene | 16.1 | 49.6 |
| Mineral oil with 20 wt% graphene | 14.5 | 43.1 |
| Mineral oil with 40 wt% graphene | 11.3 | 39.1 |
| Commercial TIM (Ice Fusion) | 16.2 | 59.3 |

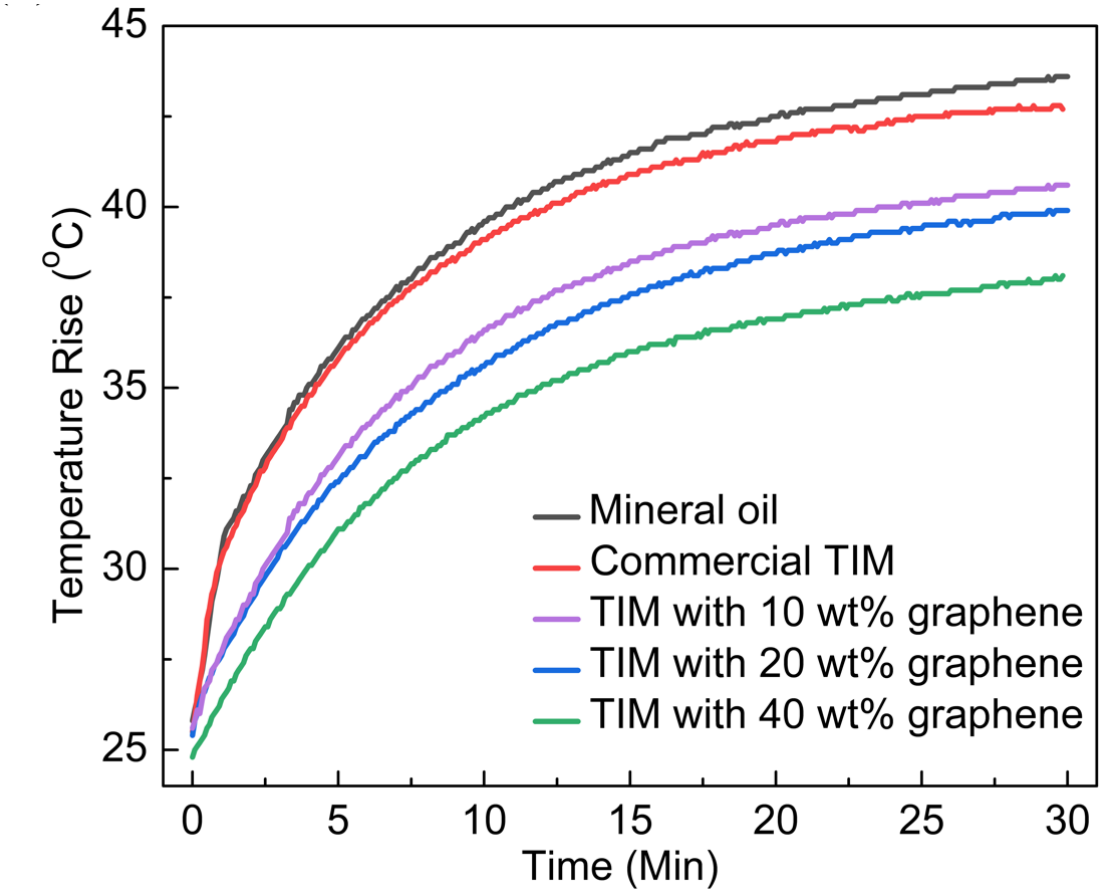


**Figure 3.5:** Temperature of the solar cell as a function of time under constant illumination of 70× suns and different noncuring TIMs. Reprinted with permission from Mahadevan, B.K; Naghibi, S.; Kargar, F.; Balandin, A.; Non-Curing Thermal Interface Materials with Graphene Fillers for Thermal Management of Concentrated Photovoltaic Solar Cells, C-Journal of Carbon Research, volume 6, p2, 2019.

The temperature rise in the solar cell was reduced by 34% using the noncured graphene-enhanced TIM with 40 wt% graphene loading as compared to that of the commercial noncured TIM under 200× suns illumination. The solar cell temperature increased from 25 ºC to 84 ºC when the commercial TIM was applied. A temperature increase of ~39 ºC, from 25 ºC to 64 ºC, was recorded when the noncured TIMs with 40 wt% graphene was used (See Figure 3.6). It was confirmed that commercial noncured TIMs

have a large variety of fillers with optimized sizes, composition and concentrations deliver the best performance. The tested in-house TIM consisted only of the mineral oil base and graphene mixture. The performance of noncured graphene-enhanced TIMs can be improved by optimizing the graphene filler size, thickness and the use of additional fillers.

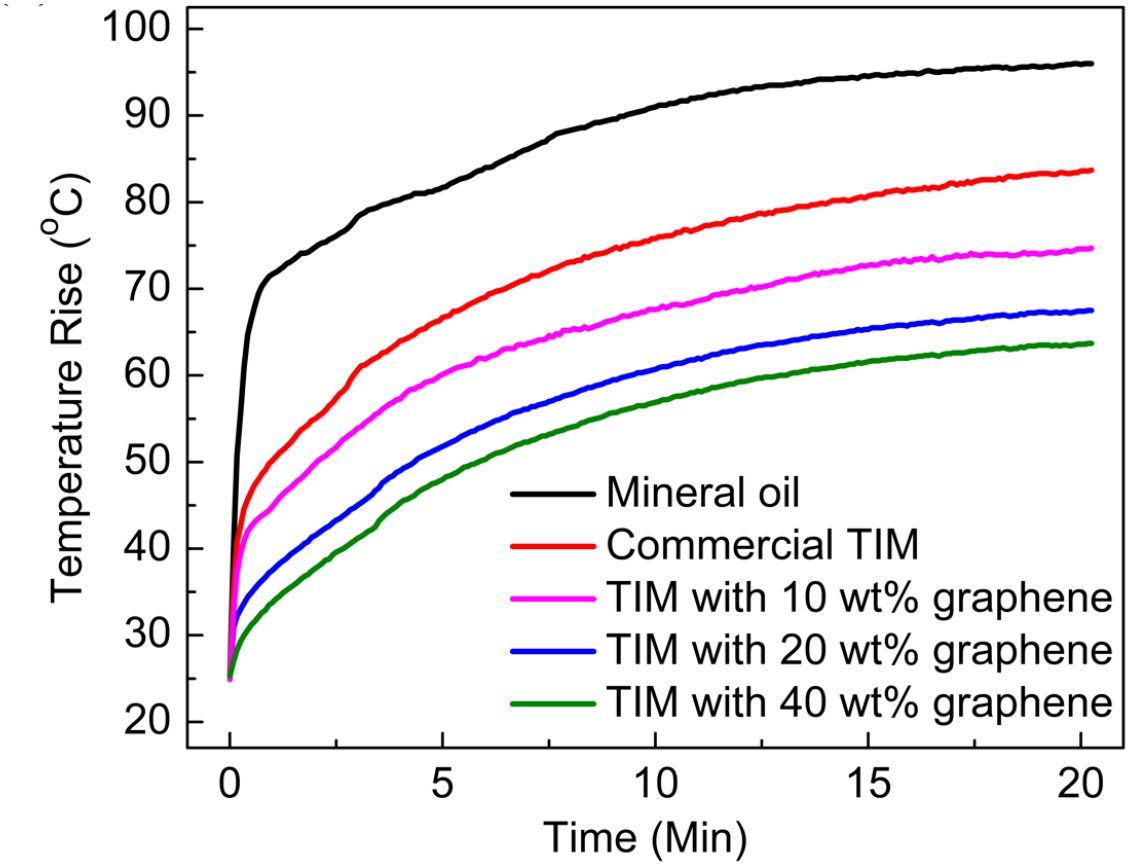


**Figure 3.6:** Temperature of the solar cell as a function of time under constant illumination of 200× suns and different noncuring TIMs. Reprinted with permission from Mahadevan, B.K; Naghibi, S.; Kargar, F.; Balandin, A.; Non-Curing Thermal Interface Materials with Graphene Fillers for Thermal Management of Concentrated Photovoltaic Solar Cells, C-Journal of Carbon Research, volume 6, p2, 2019.

## 3.3 Conclusions

In this research thesis, the feasibility of thermal management of multi-junction solar cells using graphene-enhanced noncuring thermal interface materials was studied. By using an inexpensive scalable technique, graphene fillers were incorporated in the noncuring mineral oil matrix, with the concentration up to 40 wt%. The thermal interface material was applied between a solar cell and a heat sink to improve heat dissipation. The efficiency of the solar cell has been tested using an industry standard solar simulator with concentrated light illumination at 70× suns and 200× suns. It was confirmed that the noncuring graphene enhanced thermal interface material reduces substantially the temperature rise in the solar cell and improves the open circuit voltage. The use of graphene fillers allows to achieve significant improvement in the solar cell performance compared to the commercial noncured thermal interface material. The decrease in $V_{OC}$ values was reduced up to 44% using graphene filler TIMs compared to the commercial TIM under 200× suns illumination. This was achieved due to reduction in solar cell temperature rise by 34% when graphene enhanced TIMs were utilized. The obtained results from this thesis research are important for development of the thermal management technologies for the next generation of photovoltaic solar cells.

# References


1. Chapin, D.M.; Fuller, C.S.; Pearson, G.L. A New Silicon p-n Junction Photocell for Converting Solar Radiation into Electrical Power. *J. Appl. Phys.* **1954**, *25*, 676–677.

2. Ponce, F.A. Novel Semiconductors for Sustainable Solar Energy Technologies. *J. Phys. Conf. Ser.* **2019**, *1173*.

3. Tyagi, H.; Agarwal, A.K.; Chakraborty, P.R.; Powar, S. Introduction to Advances in Solar Energy Research, 1st ed.; *Springer Singapore, SG*, **2019**; 3–11, ISBN 978-981-13-3301-9.

4. Yang, D.; Yang, R.; Priya, S.; Liu, S. (Frank) Recent Advances in Flexible Perovskite Solar Cells: Fabrication and Applications. *Angew. Chemie - Int. Ed.* **2019**, *58*, 4466–4483.

5. Xue, Q.; Xia, R.; Brabec, C.J.; Yip, H.L. Recent Advances in Semi-Transparent Polymer and Perovskite Solar Cells for Power Generating Window Applications. *Energy Environ. Sci.* **2018**, *11*, 1688–1709.

6. Rodríguez-Seco, C.; Cabau, L.; Vidal-Ferran, A.; Palomares, E. Advances in the Synthesis of Small Molecules as Hole Transport Materials for Lead Halide Perovskite Solar Cells. *Acc. Chem. Res.* **2018**, *51*, 869–880.

7. Di Carlo Rasi, D.; Janssen, R.A.J. Advances in Solution-Processed Multijunction Organic Solar Cells. *Adv. Mater.* **2019**, *31*, 1806499.

8. Zuo, C.; Bolink, H.J.; Han, H.; Huang, J.; Cahen, D.; Ding, L. Advances in Perovskite Solar Cells. *Adv. Sci.* **2016**, *3*, 1–16.

9. Du, Y.; Le, N.C.H.; Chen, D.; Chen, H.; Zhu, Y. Thermal Management of Solar Cells Using a Nano-Coated Heat Pipe Plate: An Indoor Experimental Study. *Int. J. Energy Res.* **2017**, *41*, 867–876.

10. Ciulla, G.; Lo Brano, V.; Moreci, E. Forecasting the Cell Temperature of PV Modules With an Adaptive System. *Int. J. Photoenergy* **2013**, *2013*, 192854.

11. Alonso García, M.C.; Balenzategui, J.L. Estimation of Photovoltaic Module Yearly Temperature and Performance Based on Nominal Operation Cell Temperature calculations. *Renew. Energy* **2004**, *29*, 1997–2010.

12. Radziemska, E. The Effect of Temperature on the Power Drop in Crystalline Silicon Solar Cells. *Renew. Energy* **2003,** *28*, 1-12.

13. Mageed, H.M.A. Temperature Effects on the Electrical Performance of Large Area Multicrystalline Silicon Solar Cells Using the Current Shunt Measuring Technique. *Engineering* **2010**, *2*, 888–894.

14. Brinkworth, B.J.; Cross, B.M.; Marshall, R.H.; Yang, H. Thermal Regulation of Photovoltaic Cladding. *Sol. Energy* **1997**, *61*, 169–178.

15. Brinkworth, B.J.; Sandberg, M. Design Procedure for Cooling Ducts to Minimise Efficiency Loss due to Temperature Rise in PV Arrays. *Sol. Energy* **2006**, *80*, 89–103.

16. C Chen, C.J. *Physics of Solar Energy*, 1st ed; John Wiley & Sons, Inc, Hoboken, NJ, USA **2011**, ISBN 978-0-470-64780-6.

17. Shockley, W.; Queisser, H.J. Detailed Balance Limit of Efficiency of p-n Junction Solar Cells. *J. Appl. Phys.* **1961**, *32*, 510–519.

18. Yamaguchi, M.; Takamoto, T.; Araki, K.; Ekins-Daukes, N. Multi-Junction III-V Solar Cells: Current Status and Future Potential. *Sol. Energy* **2005**, *79*, 78–85.

19. D Dimroth, F.; Kurtz, S. High-Efficiency Multijunction Solar Cells. *MRS Bull.* **2007**, *32*, 230–235.

20. Gledhill, L.K.M. High Efficiency Multi-Junction Space Solar Cells. *1995 Sp. Programs Technol. Conf.* **1995**, *32*, 1–4.

21. King, R.R.; Law, D.C.; Edmondson, K.M.; Fetzer, C.M.; Kinsey, G.S.; Yoon, H.; Sherif, R.A.; Karam, N.H. 40% Efficient Metamorphic GaInPGaInAsGe Multijunction Solar Cells. *Appl. Phys. Lett.* **2007**, *90*, 90–93.

22. De Vos, A. Detailed Balance Limit of the Efficiency of Tandem Solar Cells. *J. Phys. D. Appl. Phys.* **1980**, *13*, 839–846.

23. Geisz, J.F.; Steiner, M.A.; Jain, N.; Schulte, K.L.; France, R.M.; McMahon, W.E.; Perl, E.E.; Friedman, D.J. Building a Six-Junction Inverted Metamorphic Concentrator Solar Cell. *IEEE J. Photovoltaics* **2018**, *8*, 626–632.

24. Green, M.A.; Dunlop, E.D.; Levi, D.H.; Hohl-Ebinger, J.; Yoshita, M.; Ho-Baillie, A.W.Y. Solar Cell Efficiency Tables (Version 54). *Prog. Photovoltaics Res. Appl.* **2019**, *27*, 565–575.

25. Li, D.; Xuan, Y.; Yin, E.; Li, Q. Conversion Efficiency Gain for Concentrated Triple-Junction Solar Cell System Through Thermal Management. *Renew. Energy* **2018**, *126*, 960–968.

26. Mohammad Bagher, A. Types of Solar Cells and Application. *Am. J. Opt. Photonics* **2015**, *3*, 94–113.

27. Zweibel, K.; Mason, J.; Fthenakis, V. A Solar Grand Plan. *Sci. Am.* **2008**, *298*, 64-73.

28. Fthenakis, V.M. Life Cycle Impact Analysis of Cadmium In CdTe PV Production. *Renew. Sustain. Energy Rev.* **2004**, *8*, 303-334.

29. Eperon, G.E.; Stranks, S.D.; Menelaou, C.; Johnston, M.B.; Herz, L.M.; Snaith, H.J. Formamidinium Lead Trihalide: A Broadly Tunable Perovskite for Efficient Planar Heterojunction Solar Cells. *Energy Environ. Sci.* **2014**, *7*, 982-988.

30. Park, N.G. Perovskite Solar Cells: An Emerging Photovoltaic Technology. *Mater. Today* **2015**, *80*, 1321-1344.

31. Tributsch, H. Dye Sensitization Solar Cells: A Critical Assessment of the Learning Curve. *Coord. Chem. Rev.* **2004,** *248*, 1511-1530.

32. Hirst, L.C.; Ekins-Daukes, N.J. Fundamental Losses in Solar Cells. *Prog. Photovoltaics Res. Appl.* **2011**, *19*, 286-293.

33. S Singh, P.; Ravindra, N.M. Temperature Dependence of Solar Cell Performance - An analysis. *Sol. Energy Mater. Sol. Cells* **2012**, *101*, 36–45.

34. Matsushita, S.; Sugawara, S.; Isobe, T.; Nakajima, A. Temperature Dependence of a Perovskite-Sensitized Solar Cell: A Sensitized "Thermal" Cell. *ACS Appl. Energy Mater.* **2019**, *2*, 13–18.

35. Vadiee, E.; Fang, Y.; Zhang, C.; Fischer, A.M.; Williams, J.J.; Renteria, E.J.; Balakrishnan, G.; Honsberg, C.B. Temperature Dependence of GaSb And AlGaSb Solar Cells. *Curr. Appl. Phys.* **2018**, *18*, 752–761.

36. Taguchi, M.; Maruyama, E.; Tanaka, M. Temperature Dependence of Amorphous/Crystalline Silicon Heterojunction Solar Cells. *Jpn. J. Appl. Phys.* **2008**, *47*, 814–818.

37. Tvingstedt, K.; Deibel, C. Temperature Dependence of Ideality Factors in Organic Solar Cells and the Relation to Radiative Efficiency. *Adv. Energy Mater.* **2016**, *6*, 1–13.

38. Wysocki, J.J.; Rappaport, P. Effect of Temperature on Photovoltaic Solar Energy Conversion. *J. Appl. Phys.* **1960**, *31*, 571–578.

39. Kinsey, G.S.; Hebert, P.; Barbour, K.E.; Krut, D.D.; Cotal, H.L.; Sherif, R.A. Concentrator Multifunction Solar Cell Characteristics Under Variable Intensity and Temperature. *Prog. Photovoltaics Res. Appl.* **2008**, *16*, 503-508.

40. Sadewasser, S.; Salomé, P.M.P.; Rodriguez-Alvarez, H. Materials Efficient Deposition and Heat Management of $CuInSe_2$ Micro-Concentrator Solar Cells. *Sol. Energy Mater. Sol. Cells* **2017**, *159*, 496–502.

41. Ling, Z.; Zhang, Z.; Shi, G.; Fang, X.; Wang, L.; Gao, X.; Fang, Y.; Xu, T.; Wang, S.; Liu, X. Review on Thermal Management Systems Using Phase Change Materials for Electronic Components, Li-Ion Batteries and Photovoltaic Modules. *Renew. Sustain. Energy Rev.* **2014**, *31*, 427–438.

42. Mousavi Baygi, S.R.; Sadrameli, S.M. Thermal Management of Photovoltaic Solar Cells Using Polyethylene Glycol1000 (PEG1000) as a Phase Change Material. *Therm. Sci. Eng. Prog.* **2018**, *5*, 405–411.

43. Radwan, A.; Ookawara, S.; Ahmed, M. Thermal Management of Concentrator Photovoltaic Systems Using Two-Phase Flow Boiling in Double-Layer Microchannel Heat Sinks. *Appl. Energy* **2019**, *241*, 404–419.

44. Khan, S.A.; Sezer, N.; Ismail, S.; Koç, M. Design, Synthesis and Nucleate Boiling Performance Assessment of Hybrid Micro-Nano Porous Surfaces for Thermal Management of Concentrated Photovoltaics (CPV). *Energy Convers. Manag.* **2019**, *195*, 1056–1066.

45. Reddy, S.R.; Ebadian, M.A.; Lin, C.X. A review of PV-T systems: Thermal Management and Efficiency with Single Phase Cooling. *Int. J. Heat Mass Transf.* **2015**, *91*, 861–871.

46. Sun, X.; Silverman, T.J.; Zhou, Z.; Khan, M.R.; Bermel, P.; Alam, M.A. Optics-Based Approach to Thermal Management of Photovoltaics: Selective-Spectral and Radiative Cooling. *IEEE J. Photovoltaics* **2017**, *7*, 566–574.

47. Chauhan, A.; Tyagi, V. V.; Anand, S. Futuristic Approach for Thermal Management in Solar PV/Thermal Systems with Possible Applications. *Energy Convers. Manag.* **2018**, *163*, 314–354.

48. Ye, Z.; Li, Q.; Zhu, Q.; Pan, W. The Cooling Technology of Solar Cells Under Concentrated System. *IEEE 6th Int. Power Electron. Motion Control Conf.* **2009**, *3*, 2193–2197.

49. F Farid, M.M.; Khudhair, A.M.; Razack, S.A.K.; Al-Hallaj, S. A Review on Phase Change Energy Storage: Materials and Applications. *Energy Convers. Manag.* **2004**, *45*, 1597-1615.

50. Rabie, R.; Emam, M.; Ookawara, S.; Ahmed, M. Thermal Management of Concentrator Photovoltaic Systems Using New Configurations of Phase Change Material Heat Sinks. *Sol. Energy* **2019**, *183*, 632–652.

51. Sharma, S.; Micheli, L.; Chang, W.; Tahir, A.A.; Reddy, K.S.; Mallick, T.K. Nano-Enhanced Phase Change Material for Thermal Management of BICPV. *Appl. Energy* **2017**, *208*, 719–733.

52. Preet, S. Water and Phase Change Material Based Photovoltaic Thermal Management Systems: A Review. *Renew. Sustain. Energy Rev.* **2018**, *82*, 791–807.

53. Browne, M.C.; Norton, B.; McCormack, S.J. Phase Change Materials for Photovoltaic Thermal Management. *Renew. Sustain. Energy Rev.* **2015**, *47*, 762–782.

54. Zalba, B.; Marín, J.M.; Cabeza, L.F.; Mehling, H. Review on Thermal Energy Storage with Phase Change: Materials, Heat Transfer Analysis and Applications. *Appl. Therm. Eng.* **2003**, *23*, 251-283.

55. Sharma, A.; Tyagi, V. V.; Chen, C.R.; Buddhi, D. Review on Thermal Energy Storage with Phase Change Materials and Applications. *Renew. Sustain. Energy Rev.* **2009**, *13*, 318-345.

56. Hasan, A.; McCormack, S.J.; Huang, M.J.; Norton, B. Evaluation of Phase Change Materials for Thermal Regulation Enhancement of Building Integrated Photovoltaics. *Sol. Energy* **2010**, *84*, 1601–1612.

57. Huang, M.J.; Eames, P.C.; Norton, B. Phase Change Materials for Limiting Temperature Rise in Building Integrated Photovoltaics. *Sol. Energy* **2006**, *80*, 1121–1130.

58. Du, D.; Darkwa, J.; Kokogiannakis, G. Thermal Management Systems for Photovoltaics (PV) Installations: A Critical Review. *Sol. Energy* **2013**, *97*, 238–254.

59. Renteria, J.; Nika, D.; Balandin, A. Graphene Thermal Properties: Applications in Thermal Management and Energy Storage. *Appl. Sci.* **2014**, *4*, 525–547.

60. Goli, P.; Legedza, S.; Dhar, A.; Salgado, R.; Renteria, J.; Balandin, A.A. Graphene-Enhanced Hybrid Phase Change Materials for Thermal Management of Li-Ion Batteries. *J. Power Sources* **2014**, *248*, 37–43.

61. Prasher, R.; Chiu, C.P. Thermal Interface Materials. *Mater. Adv. Packag.* **2016**, *10*, 511–535.

62. Zhang, K.; Chai, Y.; Yuen, M.M.F.; Xiao, D.G.W.; Chan, P.C.H. Carbon Nanotube Thermal Interface Material for High-Brightness Light-Emitting-Diode Cooling. *Nanotechnology* **2008**, *19*, 215706.

63. Renteria, J.; Legedza, S.; Salgado, R.; Balandin, M.P.; Ramirez, S.; Saadah, M.; Kargar, F.; Balandin, A.A. Magnetically-Functionalized Self-Aligning Graphene Fillers for High-Efficiency Thermal Management Applications. *Mater. Des.* **2015**, *88*, 214–221.

64. Malekpour, H.; Chang, K.H.; Chen, J.C.; Lu, C.Y.; Nika, D.L.; Novoselov, K.S.; Balandin, A.A. Thermal Conductivity of Graphene Laminate. *Nano Lett.* **2014**, *14*, 5155–5161.

65. Yan, Z.; Nika, D.L.; Balandin, A.A. Thermal Properties of Graphene and Few-Layer Graphene: Applications in Electronics. *IET Circuits, Devices Syst.* **2015**, *9*, 4–12.

66. Li, X.; Yang, R. Effect Of Lattice Mismatch on Phonon Transmission and Interface Thermal Conductance Across Dissimilar Material Interfaces. *Phys. Rev. B - Condens. Matter Mater. Phys.* **2012**, *86*, 054305.

67. Due, J.; Robinson, A.J. Reliability of Thermal Interface Materials: A Review. *Proc. of the Appl. Ther. Engi.;* **2013**, *50*, 455-463.

68. Shahil, K.M.F.; Balandin, A.A. Thermal Properties of Graphene And Multilayer Graphene: Applications in Thermal Interface Materials. *Solid State Commun.* **2012**, *152*, 1331–1340.

69. Shahil, K.M.F.; Balandin, A.A. Graphene-Multilayer Graphene Nanocomposites as Highly Efficient Thermal Interface Materials. *Nano Lett.* **2012**, *12*, 861–867.

70. I Incropera, F.P.; Dewitt, D.P.; Bergman, T.L.; Lavine, A.S. *Fundamentals of Heat and Mass Transfer*, 6th ed; John Wiley & Sons, Inc, Hoboken, NJ, USA, **2006**, ISBN 978-0-471-45728-2.

71. Nika, D.L.; Pokatilov, E.P.; Askerov, A.S.; Balandin, A.A. Phonon Thermal Conduction in Graphene: Role of Umklapp and Edge Roughness Scattering. *Phys. Rev. B - Condens. Matter Mater. Phys.* **2009**, *79*, 1–12.

72. Balandin, A.A.; Nika, D.L.; Ghosh, S.; Pokatilov, E.P. Lattice Thermal Conductivity of Graphene Flakes: Comparison with Bulk Graphite. *Appl. Phys. Lett.* **2009**, *94*, 3–5.

73. Ghosh, S.; Bao, W.; Nika, D.L.; Subrina, S.; Pokatilov, E.P.; Lau, C.N.; Balandin, A.A. Dimensional Crossover of Thermal Transport in Few-Layer Graphene. *Nat. Mater.* **2010**, *9*, 555–558.

74. Ghosh, S.; Nika, D.L.; Pokatilov, E.P.; Balandin, A.A. Heat Conduction in Graphene: Experimental Study and Theoretical Interpretation. *New J. Phys.* **2009**, *11*, 095012.

75. Balandin, A.A. Thermal Properties of Graphene and Nanostructured Carbon Materials. *Nat. Mater.* **2011**, *10*, 569–581.

76. Balandin, A.A.; Ghosh, S.; Nika, D.L.; Pokatilov, E.P. Thermal Conduction in Suspended Graphene Layers. *Fullerenes Nanotub. Carbon Nanostructures* **2010**, *18*, 474–486.

77. Goyal, V.; Balandin, A.A. Thermal Properties of the Hybrid Graphene-Metal Nano-Micro-Composites: Applications in Thermal Interface Materials. *Appl. Phys. Lett.* **2012**, *100*, 073113.

78. Loeblein, M.; Tsang, S.H.; Pawlik, M.; Phua, E.J.R.; Yong, H.; Zhang, X.W.; Gan, C.L.; Teo, E.H.T. High-Density 3D-Boron Nitride and 3D-Graphene for High-Performance Nano-Thermal Interface Material. *ACS Nano* **2017**, *11*, 2033–2044.

79. Tang, B.; Hu, G.; Gao, H.; Hai, L. Application of Graphene as Filler to Improve Thermal Transport Property of Epoxy Resin for Thermal Interface Materials. *Int. J. Heat Mass Transf.* **2015**, *85*, 420–429.

80. Park, W.; Guo, Y.; Li, X.; Hu, J.; Liu, L.; Ruan, X.; Chen, Y.P. High-Performance Thermal Interface Material Based on Few-Layer Graphene Composite. *J. Phys. Chem. C* **2015**, *119*, 26753–26759.

81. Kargar, F.; Barani, Z.; Balinskiy, M.; Magana, A.S.; Lewis, J.S.; Balandin, A.A. Dual-Functional Graphene Composites for Electromagnetic Shielding and Thermal Management. *Adv. Electron. Mater.* **2019**, *5*, 35–39.

82. Kargar, F.; Barani, Z.; Salgado, R.; Debnath, B.; Lewis, J.S.; Aytan, E.; Lake, R.K.; Balandin, A.A. Thermal Percolation Threshold and Thermal Properties of Composites with High Loading of Graphene and Boron Nitride Fillers. *ACS Appl. Mater. Interfaces* **2018**, *10*, 37555–37565.

83. Lewis, J.S.; Barani, Z.; Magana, A.S.; Kargar, F.; Balandin, A.A. Thermal and Electrical Conductivity Control in Hybrid Composites with Graphene and Boron Nitride Fillers. *Mater. Res. Express* **2019**, *6*, 085325.

84. Barani, Z.; Mohammadzadeh, A.; Geremew, A.; Huang, C.Y.; Coleman, D.; Mangolini, L.; Kargar, F.; Balandin, A.A. Thermal Properties of the Binary-Filler Hybrid Composites with Graphene and Copper Nanoparticles. *Adv. Funct. Mater.* **2019**, *1904008*, 1–11.

85. Lv, P.; Tan, X.W.; Yu, K.H.; Zheng, R.L.; Zheng, J.J.; Wei, W. Super-Elastic Graphene/Carbon Nanotube Aerogel: A Novel Thermal Interface Material with Highly Thermal Transport Properties. *Carbon N. Y.* **2016**, *99*, 222–228.

86. Naghibi, S.; Kargar, F.; Wright, D.; Huang, C.Y.T.; Mohammadzadeh, A.; Barani, Z.; Salgado, R.; Balandin, A.A. Noncuring Graphene Thermal Interface Materials for Advanced Electronics. *Adv. Electron. Mater.* **2020**, 1901303.

87. Riordan, C.; Hulstrom, R. What Is An Air Mass 1.5 Spectrum? *IEEE Photovoltaic Specialists Conferenc*e, Kissimmee, FL, USA **1990**, *2*, 1085-1088.

88. Oriel, Newport Corporation. In *Oriel Product Training Manual* **2006**, 9.

89. LongWin North America Laboratory TIM Tester. In *TIM Tester Training manual* **2019**, 9.

90. SimpleVIS Kinematic Viscometer, Cannon Instruments. In *SimpleVIS Kinematic Viscometer Reference Guide* **2012**, 15.

91. Solar Cell Type 3C42C, AZUR Space. In *Solar Cell Type 3C42C- Data Sheet (HNR 0003878-00-00)* **2014**, 4.

92. xGnP® Graphene Nanoplatelets – Grade H, XG-Sciences. In *xGnP® Graphene Nanoplatelets – Grade H , Product Specification Sheet* **2019**, 1.

93. Huang, M.J.; Eames, P.C.; Norton, B.; Hewitt, N.J. Natural Convection in an Internally Finned Phase Change Material Heat Sink for the Thermal Management of Photovoltaics. *Sol. Energy Mater. Sol. Cells* **2011**, *95*, 1598-1603.

94. Hasan, A.; Sarwar, J.; Shah, A.H. Concentrated Photovoltaic: A Review of Thermal Aspects, Challenges and Opportunities. *Renew. Sustain. Energy Rev.* **2018**, *94*, 835-852.

95. Coll, S.J.; Rodgers, P.; Eveloy, V. Thermal Management of Solar Photovoltaics Modules for Enhanced Power Generation. *Renew. Energy* **2015**, *82*, 14-20.

96. Saadah, M.; Hernandez, E.; Balandin, A.A. Thermal Management of Concentrated Multi-Junction Solar Cells with Graphene-Enhanced Thermal Interface Materials. *Appl. Sci.* **2017**, *7*, 589.